



BRNO UNIVERSITY OF TECHNOLOGY

VYSOKÉ UČENÍ TECHNICKÉ V BRNĚ

FACULTY OF MECHANICAL ENGINEERING

FAKULTA STROJNÍHO INŽENÝRSTVÍ

INSTITUTE OF PHYSICAL ENGINEERING

ÚSTAV FYZIKÁLNÍHO INŽENÝRSTVÍ

APPLICATIONS OF METALLIC PROBE FOR THE CONTROL OF OPTICAL PROCESSES AND NEAR-FIELD IMAGING

VYUŽITÍ KOVOVÉ SONDY PRO OVLÁDÁNÍ OPTICKÝCH PROCESŮ A ZOBRAZOVÁNÍ V BLÍZKÉM POLI

MASTER'S THESIS

DIPLOMOVÁ PRÁCE

AUTHOR

AUTOR PRÁCE

Bc. Pavel Gallina

SUPERVISOR

VEDOUCÍ PRÁCE

Mgr. Vlastimil Křápek, Ph.D.

BRNO 2018

Master's Thesis Assignment

Institut: Institute of Physical Engineering
Student: **Bc. Pavel Gallina**
Degree programm: Applied Sciences in Engineering
Branch: Physical Engineering and Nanotechnology
Supervisor: **Mgr. Vlastimil Křápek, Ph.D.**
Academic year: 2017/18

As provided for by the Act No. 111/98 Coll. on higher education institutions and the BUT Study and Examination Regulations, the director of the Institute hereby assigns the following topic of Master's Thesis:

Applications of metallic probe for the control of optical processes and near-field imaging

Brief description:

Metallic tip located close to the planar sample forms an optical resonator with enhanced electromagnetic field in its vicinity, which consequently affects related optical processes (e.g. light absorption, Raman scattering, etc.).

Spatial resolution of traditional far-field optical microscopy is limited by the wavelength of involved radiation (diffraction limit). Considerably better resolution is offered by near-field methods. Scanning near-field optical microscopy is a prominent near-field technique utilizing a probe formed by an optical fibre terminated with a metallic tip. Near field scattered at the tip results into a far field propagating through the fibre, whose intensity and wavelength is characterized by a connected spectrometer.

The role of the metallic probe in optical processes enhancement and near-field imaging will be studied with a numeric modelling. In the case of optical processes, the influence of localised surface plasmon polaritons in metallic tip on the infrared vibronic spectroscopy (Raman scattering, infrared absorption) will be investigated. In the case of imaging, the model of a structure with a non-trivial near field will be created and the mechanism of the interaction with a metallic tip will be studied. Parameters of the tip will be modified to allow detection of specific components of the field.

Master's Thesis goals:

To describe the influence of the metallic tip on the intensity of molecular vibronic spectra (Raman scattering, infrared absorption).

To study the effect of the graphene layer to the enhancement of vibronic spectra.

To describe the interaction between the tip and near field in scanning near-field spectroscopy with a numeric model.

To find the parameters of the tip selectively sensitive to specific components of the near field.

Recommended bibliography:

NOVOTNY, L. a HECHT, B., Principles of Nano-Optics, 2. vydání, Cambridge, 2012.

DVOŘÁK, P., NEUMAN, J., BŘÍNEK, L. aj., Control and near-field detection of surface plasmon interference patterns. Nano letters, ročník 13, č. 6, 2013: s. 2558 – 2563.

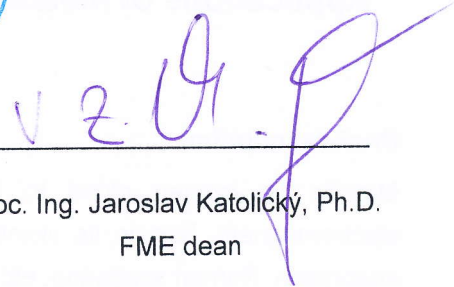
STILES, P. L., DIERINGER, J. A., SHAH, N. C., and DUYNE, R. P. V., Surface-enhanced raman spectroscopy. Annual Review of Analytical Chemistry, svazek 1, 2008: s. 601 – 626.

Students are required to submit the thesis within the deadlines stated in the schedule of the academic year 2017/18.

In Brno, 3. 11. 2017



prof. RNDr. Tomáš Šikola, CSc.
Director of the Institute



doc. Ing. Jaroslav Katolický, Ph.D.
FME dean

Summary

The main subject of this master's thesis are electromagnetic simulations using the finite element method (FEM) to investigate the influence of graphene on tip-enhanced Raman spectroscopy (TERS) and surface-enhanced infrared absorption spectroscopy (SEIRA) and to inspect the sensitivity of the scanning near-field optical microscope (SNOM) probe to the components of electromagnetic field depending on the parameters of the probe (the aperture diameter in the metallic coating). First, the calculation of TERS system composed of a silver tip located above a gold substrate with a thin layer of molecules is carried out to understand the principles of TERS. Then the graphene layer is added on top of the molecules to examine its influence in visible (TERS) and infrared (SEIRA) region of the spectrum. The second part focuses on the calculations of energy flux through a metal coated glass fiber forming a SNOM tip interacting with the near-field of surface plasmon polaritons. Here, we consider a gold layer with four slits arranged in a square pattern on a glass substrate serving as a source of a surface plasmon polariton standing wave with spatially separated maxima of in-plane and out-of-plane electric field components.

Abstrakt

Hlavním předmětem této diplomové práce jsou elektromagnetické simulace pomocí metody konečných prvků (FEM) k vyšetření vlivu grafenu na hrotem zesílenou Ramanovu spektroskopii (TERS) a povrchem zesílenou infračervenou absorpční spektroskopii (SEIRA) a k prozkoumání citlivosti sondy skenovacího optického mikroskopu blízkého pole (SNOM) ke složkám elektromagnetického pole v závislosti na parametrech sondy (průměru apertury v pokovení). Nejprve je proveden výpočet TERS systému složeného ze stříbrného hrotu nacházejícího se nad zlatým substrátem s tenkou vrstvou molekul, jehož účelem je porozumění principů TERS. Poté je na molekuly přidána grafenová vrstva, aby se prozkoumal její vliv ve viditelné (TERS) a infračervené (SEIRA) oblasti spektra. Druhá část práce se zabývá výpočty energiového toku SNOM hrotem složeným z pokoveného skleněného vlákna interagujícím s blízkým polem povrchových plasmonových polaritonů. Zde uvažujeme zlatou vrstvu se čtyřmi štěrbinami uspořádanými do čtverce na skleněném substrátu sloužícími jako zdroj stojatého vlnění povrchových plasmonů s prostorově oddělenými maximy složek elektrického pole orientovanými rovnoběžně či kolmo na vzorek.

Ve výpočtech hrotem zesílené spektroskopie zjišťujeme, že grafen přispívá pouze malým dílem k zesílení pole ve viditelné oblasti spektra, ovšem v infračervené oblasti má grafen vliv pro záření s energií menší než dvojnásobek Fermiho energie grafenu, pro kterou je hodnota zesílení pole větší než v případě výpočtu bez grafenu. Avšak pro velmi vysoké vlnové délky zesílení pole v přítomnosti grafenu klesá pod (konstantní) hodnotu pro případ bez grafenu.

Při studiu citlivosti SNOM hrotu k jednotlivým složkám pole sledujeme, že pro hrot se zlatým pokovením je energiový tok skleněným jádrem hrotu kombinací příspěvků energie prošlé aperturou a periodické výměny energie mezi povrchovým plasmonem šířícím se po vnějším okraji pokovení a módy propagujícími se v jádře. Dále zjišťujeme, že hroty s malou aperturou (či bez apertury) jsou více citlivé na složku elektrického pole orientovanou kolmo ke vzorku (rovnoběžně s osou hrotu), zatímco hroty s velkou aperturou sbírají spíše signál ze složky rovnoběžné s povrchem vzorku. V případě hrotu s hliníkovým pokovením jsou hroty citlivější ke složce pole rovnoběžné s povrchem, což je způsobeno slabším průnikem pole skrze pokovení.

Keywords

surface plasmon polaritons (SPP), plasmonics, tip-enhanced Raman spectroscopy (TERS), graphene-enhanced Raman spectroscopy (GERS), graphene, surface-enhanced infrared absorption spectroscopy (SEIRA), scanning near-field optical microscopy (SNOM), SNOM tip sensitivity, finite element method (FEM)

Klíčová slova

povrchové plasmonové polaritony, plasmonika, hrotem zesílená Ramanova spektroskopie, grafenem zesílená Ramanova spektroskopie, grafen, povrchem zesílená infračervená absorpční spektroskopie, skenovací optický mikroskop blízkého pole, citlivost SNOM hrotu, metoda konečných prvků

GALLINA, P. *Applications of metallic probe for the control of optical processes and near-field imaging*. Brno: Brno University of Technology, Faculty of Mechanical Engineering, 2018. 54 p. Supervisor Mgr. Vlastimil Křápek, Ph.D.

DECLARATION

I hereby declare that I have elaborated my master's thesis entitled *Applications of metallic probe for the control of optical processes and near-field imaging* independently, under the supervision of Mgr. Vlastimil Křápek, Ph.D., and using the technical literature and other sources of information which are all properly cited and listed in the bibliography.

Brno 25.5.2018

..... 
Bc. Pavel Gallina

ACKNOWLEDGEMENT

Primarily, I would like to thank my supervisor Mgr. Vlastimil Křápek, Ph.D., for his guidance, helpful comments and corrections. I would like to also express my gratitude to dr. Rubén Esteban and prof. Javier Aizpurua for their supervision during my stay at Center for Material Physics in San Sebastián where I began the work on this thesis. My thanks also belong to dr. Luca Bergamini and Ing. Jakub Zlámal, Ph.D., for the help with the implementation of calculations and lastly to my colleagues at Institute of Physical Engineering at BUT and at Center for Material Physics in San Sebastián for many useful discussions.

I would like to thank my family, especially my parents, and my friends for their support and encouragement during my studies and my entire life.

Bc. Pavel Gallina

Contents

1	Introduction	2
1.1	Plasmon polaritons	3
1.1.1	Propagating surface plasmon polaritons in metals	4
1.1.2	Propagating surface plasmon polaritons in graphene	6
1.1.3	Localized surface plasmon polaritons in metallic particles	8
1.2	Raman spectroscopy	11
1.2.1	Surface-enhanced and tip-enhanced Raman spectroscopy	12
1.2.2	Graphene-enhanced Raman spectroscopy	12
1.3	Surface-enhanced infrared absorption spectroscopy	13
1.4	Scanning near-field optical microscopy	13
1.4.1	Sensitivity of SNOM tips to components of electromagnetic field	15
2	Model	17
2.1	Model for tip-enhanced Raman and infrared absorption spectroscopy calculations	17
2.2	Model for scanning near-field optical microscope calculations	18
3	Methods	21
3.1	Introduction to the finite element method	21
3.2	Comparing numerical and analytical results: gold sphere	23
3.3	Comparing numerical and analytical results: multilayer system	24
4	Tip-enhanced spectroscopy calculations	25
4.1	Tip enhanced Raman spectroscopy calculations	25
4.1.1	Effect of the tip enhancement	25
4.1.2	Effect of graphene	30
4.2	Effect of graphene in SEIRA	32
5	Scanning near-field optical microscope calculations	36
6	Conclusion	43
	Appendices	51
A	Analytical model for a multilayer system	52

1. Introduction

Spectroscopic techniques such as Raman spectroscopy [1, 2] and infrared absorption spectroscopy [3] allow to examine the properties of materials, for example for detection and analysis of molecules. Both of these methods study the rotational and vibrational modes of molecules at energies $\hbar\Omega_i \approx 100$ meV in the mid-infrared region (often called the molecular fingerprint) that is unique to every compound and it can thus be used to recognize specific molecules. More specifically, Raman spectroscopy is based on the exchange of energy between the molecular vibrations in the mid-infrared and laser light at frequency ω in the visible or near-infrared region and subsequent emission at the Stokes ($\omega - \Omega_i$) and anti-Stokes ($\omega + \Omega_i$) frequencies in the spectrum. In infrared absorption spectroscopy, on the other hand, the signal of interest is the direct absorption of infrared light of energy $\hbar\omega$ close to the molecular transition energy $\hbar\Omega_i$. Although these techniques have been widely used, the weak interaction of the molecules with the incoming light means that the signal is usually too weak for studying single molecules or low concentrations of materials.

A widely used approach for enhancing the spectroscopic signal is making use of surface plasmon polaritons (SPPs) [4] excited at rough metallic surfaces. Surface plasmon polaritons are excitations arising from the interaction between light and the collective oscillations of the free electrons in a metal (or novel 2D materials such as graphene), which amplify and confine the electromagnetic field in a small region near the metal and thus enhance the interaction with nearby molecules. We distinguish two types of SPPs: propagating SPPs in flat metallic surfaces and localized SPPs in finite metallic structures (such as particles). The techniques that exploit SPPs to amplify the spectroscopic Raman or infrared absorption signal are called surface-enhanced Raman spectroscopy (SERS) [5, 6, 7, 8] or surface-enhanced infrared absorption spectroscopy (SEIRA) [8, 9], respectively. Besides the plasmonic enhancement, SERS and SEIRA can also benefit from a chemical enhancement when the molecule is in direct contact with the metal [10]. When localized plasmons are excited at the apex of a metallic tip near a metallic substrate, SERS is often called TERS (tip-enhanced Raman spectroscopy) [11].

Furthermore, in recent years it has been also shown that the spectroscopic signal can be amplified by placing graphene in contact with the studied molecules, in what is called graphene-enhanced Raman spectroscopy (GERS) [12]. Because of the smooth surface of the graphene (even though some roughness may appear as it copies the underlying substrate) and high optical transmissivity, the largest contribution to the signal is believed to come from a chemical mechanism such as charge transfer rather than from an electromagnetic mechanism (excitation of plasmons as in SERS) [12, 13].

Scanning near-field optical microscopy (SNOM) [4, 14, 15] is a technique frequently used for high resolution imaging of objects with features smaller than the wavelength of light. This method overcomes the diffraction limit of light by utilizing a small tip that is scanned over the sample, acting as a source or a detector of the near-field. The tips are either tapered glass fibers coated with metal with a small subwavelength aperture at the apex [15], which allow to guide the light to and from a specific site on the sample through the fiber, or dielectric atomic force microscope probes [16] acting as a subwavelength scatterer. The area of application of SNOM is thus imaging of e.g. surface plasmon polaritons (SPPs) [17, 18], fluorescent molecules [19] or quantum dots [20]. The mechanism by which the near-field above the sample around the tip couples with the propagating modes in a fiber core of a standard SNOM tip with an aperture is based on the electric

field passing through both the aperture and the coating, making it hard to discern these two contributions and leading to a disagreement whether the in-plane [21, 22, 23] or the out-of-plane [18, 24, 25] component of the electric field are detected when the probe is used in a collection (detection) mode.

In this thesis, we first perform electromagnetic calculations to study the Raman signal in TERS experiments where the molecules are covered by a graphene layer, thus potentially combining the TERS and GERS effect (inspired by the experimental work of our collaborators at HU Berlin (group of Prof. J. P. Rabe) and ETH Zurich (group of Prof. R. Zenobi) [26, 27]). Calculations of SEIRA are also used to show the effect of graphene when the excitation is in the infrared region. The second part of the work (inspired by experiments of our collaborators at Institute of Physical Engineering at BUT [18, 24]) consists of electromagnetic simulations of a SNOM tip with an aperture detecting a SPP standing wave to investigate the sensitivity of the tip to the components of the electromagnetic field. Before describing the exact geometries studied in chapter 2, the numerical methods in chapter 3 and the results in chapters 4 and 5, we introduce in more detail the basic principles behind SPPs, SERS, SEIRA and SNOM.

1.1. Plasmon polaritons

The response of materials to the electromagnetic field can be described by the dielectric function ε [4, 14, 28]. For an ideal free electron gas in metals we can derive its relative permittivity ε_m by solving the equation of motion of free electrons driven by an external harmonic field with a frequency ω , giving us Drude model [4, 14]

$$\varepsilon_m = 1 - \frac{\omega_p^2}{\omega^2 + i\Gamma\omega}, \quad (1.1)$$

where Γ is the damping coefficient and ω_p is the plasma frequency defined as

$$\omega_p = \sqrt{\frac{ne^2}{m_{\text{eff}}\varepsilon_0}}, \quad (1.2)$$

with n being the concentration of electrons, e and m_{eff} the electron charge and effective mass, and ε_0 the vacuum permittivity. For example, in the case of gold with $n = 5.9 \cdot 10^{22} \text{ cm}^{-3}$ [29] and $m_{\text{eff}} = 0.99m_0$ [30] (with m_0 being the free electron mass), the plasma frequency is $\omega_p = 1.38 \cdot 10^{16} \text{ s}^{-1}$ (corresponding to energy $\hbar\omega_p = 9.06 \text{ eV}$ and plasma wavelength $\lambda_p = 137 \text{ nm}$). At the plasma frequency ω_p (corresponding to $\varepsilon = 0$) the free electrons inside a metal exhibit a resonant collective oscillation which we call bulk plasmon (or volume plasmon). Bulk plasmons can be excited by electrons in electron energy loss spectroscopy (EELS) measurements [31], where a beam of high energetic electrons penetrates through the metal and some of the electrons lose part of their energy through inelastic collisions. However, bulk plasmons are longitudinal waves of relatively low momentum that cannot be excited by (transverse) photons with larger momentum.

Nonetheless, as we are interested in applications associated with enhancement of the electric field near the surfaces of metals, we describe in the next subsection the surface plasmon polaritons, which are excited at the interface of a metal with a surrounding medium and can couple with light.

1.1. PLASMON POLARITONS

1.1.1. Propagating surface plasmon polaritons in metals

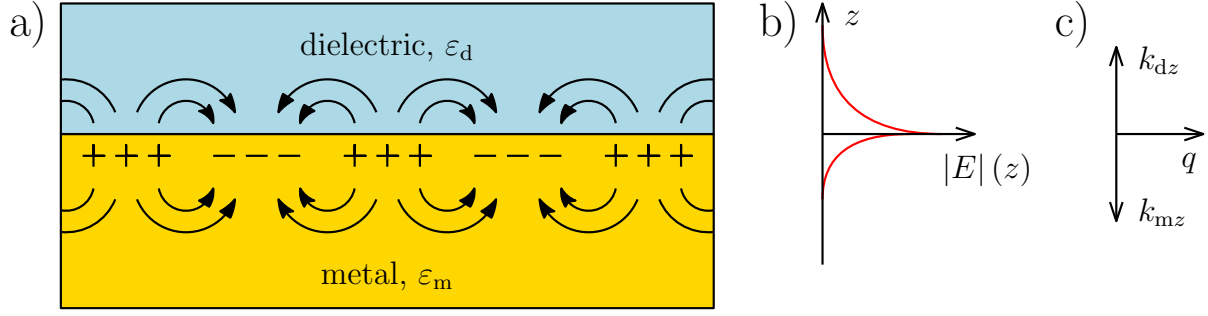


Figure 1.1: Scheme of the surface plasmon polariton. (a) Scheme of charge distribution and field lines for surface plasmon polariton. (b) The electric field of SPP decays exponentially in both materials, as represented in the scheme. (c) Definition of the component of the wave vector perpendicular to the interface, k_{dz} or k_{mz} for the dielectric and metal, respectively, and the parallel component q .

Surface plasmons polaritons (SPPs) are surface waves that can be excited at the interface between a metallic substrate and a dielectric material on top [4, 14] (Fig. 1.1). Perhaps the easiest way to derive the conditions at which the SPPs are excited is by analyzing the Fresnel coefficient of reflection of light from a dielectric-metal interface. When the light is p-polarized or, equivalently, transverse magnetic (TM, corresponding to the polarization when the magnetic field is perpendicular to the plane of incidence defined by the direction of propagation and the interface normal) we obtain

$$r_p = \frac{n_m \cos \theta_i - n_d \cos \theta_t}{n_m \cos \theta_i + n_d \cos \theta_t} = \frac{\epsilon_m k_{dz} - \epsilon_d k_{mz}}{\epsilon_m k_{dz} + \epsilon_d k_{mz}}, \quad (1.3)$$

where n_m and n_d are the refractive indices of the metal and the dielectric (corresponding permittivities are $\epsilon_m = n_m^2$ and $\epsilon_d = n_d^2$), θ_i and θ_t are the angles of incidence and refraction and k_{mz} and k_{dz} are the corresponding normal components of the wave vectors. We have written the reflection coefficient in two different ways because the expression in terms of angles may be more intuitive but using k_{mz} and k_{dz} is more practical for our purposes (as plasmons involve evanescent waves that correspond to complex angles). We only consider p-polarization because it is not possible to excite SPPs with the orthogonal s-polarization [4, 14]. The excitation of a plasmonic mode corresponds to the condition in which the response diverges (the mode is self-sustained) and this corresponds to having a pole of the right hand side of Eq. 1.3, i.e. the equation

$$\epsilon_m k_{dz} + \epsilon_d k_{mz} = 0, \quad (1.4)$$

which gives the relation between k_{mz} and k_{dz} . The parallel component of the wave vector q is the same in both media (otherwise it is not possible to fulfil the boundary conditions

at all points of the interface). For wave number in both media the following equations hold

$$\begin{aligned} k_d^2 &= \varepsilon_d \frac{\omega^2}{c^2} = q^2 + k_{dz}^2, \\ k_m^2 &= \varepsilon_m \frac{\omega^2}{c^2} = q^2 + k_{mz}^2, \end{aligned} \quad (1.5)$$

where c is the speed of light in vacuum.

By combining Eqs. 1.4 and 1.5 we can derive the general formula for the dispersion relation of the SPPs

$$q = \frac{\omega}{c} \sqrt{\frac{\varepsilon_m(\omega)\varepsilon_d}{\varepsilon_m(\omega) + \varepsilon_d}}. \quad (1.6)$$

To illustrate the behaviour of this equation, we specify for simplicity the dielectric as vacuum ($\varepsilon_d = 1$) and substitute the dielectric function of the metal by the Drude model without losses (Eq. 1.1 with $\Gamma = 0$). We obtain

$$q = \frac{\omega}{c} \sqrt{\frac{\omega^2 - \omega_p^2}{2\omega^2 - \omega_p^2}}, \quad (1.7)$$

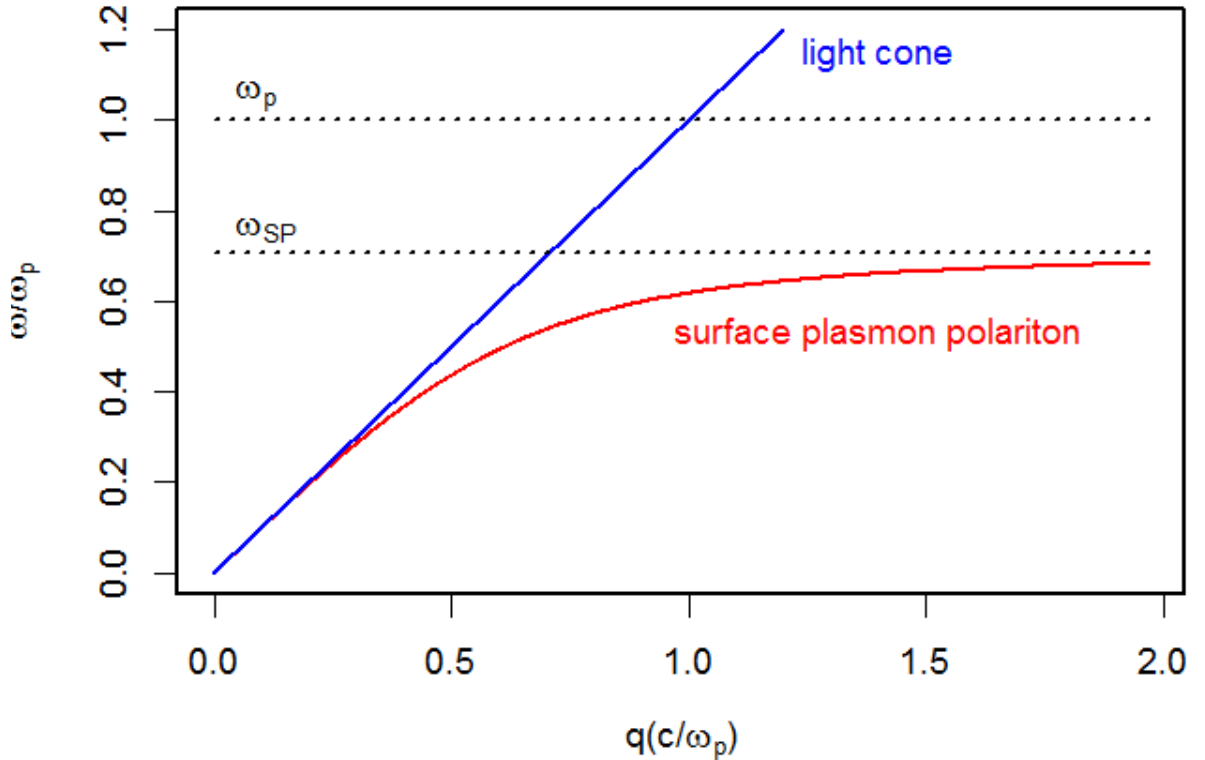


Figure 1.2: Dispersion relation of a surface plasmon polariton (red line). The blue line corresponds to the light cone following $\omega = cq/n_d$. The parallel wave number q of the SPP is always larger than the wave number of light, giving the SPP an evanescent character. The horizontal dashed lines correspond to the surface plasmon frequency ω_{SP} and the bulk plasmon frequency ω_p . There is no SPP above the surface plasmon frequency. The results were calculated for a lossless Drude model and $\varepsilon_d = 1$.

1.1. PLASMON POLARITONS

which is displayed in Fig. 1.2 (red line) together with the light cone ($\omega = cq/n_d$, blue line). The light cone gives for each frequency ω the maximum parallel wave number of a propagating plane wave, found for the incident angle $\theta_d = \pi/2$ where $q = k_d \sin(\theta_d) = k_d$. For a small frequency ω (energy $\hbar\omega$) the parallel wave number q is asymptotically close to the light cone, but for an increasing frequency the parallel wave number becomes much larger than for the light cone, approaching infinity for frequency ω_{SP} . ω_{SP} is called the surface plasmon frequency and can be found from the pole of Eq. 1.7 (i.e. the frequency at which q grows to infinity) giving $\omega_{\text{SP}} = \omega_p/\sqrt{2}$. Because q is larger than the wave number in the dielectric k_d , the perpendicular component k_{dz} (and also k_{mz} in metal, where ϵ_m is negative) is imaginary according to Eq. 1.5. As a result, SPP is an evanescent wave, decaying along the normal of the interface, and thus confining the plasmonic energy near the interface. It is worth mentioning that in real metals there is always a damping present ($\Gamma \neq 0$), hence q of the SPP is imaginary and the plasmon also decays as it propagates along the interface.

From the graph in Fig. 1.2 we can deduce that it is not possible to excite SPP in a flat metallic surface directly with a non-evanescent plane wave, since the light and the SPP of the same energy $\hbar\omega$ never have the same in-plane component q of the wave vector. In order to overcome this momentum mismatch different approaches can be used [4, 14]. The SPP can be excited by an evanescent wave which, following Eq. 1.5, enables to obtain q larger than k (since k_z is imaginary); this evanescent illumination can be achieved in the Otto configuration [32] by using the total internal reflection from a prism face that is near the metal surface, or in the Kretschmann configuration [33], where the light reflected from a prism-metal interface tunnels through the thin metal layer and excites SPP on the metal surface. Another technique of exciting the SPPs is provision of extra momentum by a plasmonic structure, as it is often done by creating a grating on the surface of the metal [34] or by introducing a small object near the interface (e.g. a nanoparticle, a metallic tip, or a hole or a slit in the metal layer), thus exciting the SPP in the near-field [35]. Similarly to bulk plasmons, one can also excite surface plasmon polaritons with a beam of high energetic electrons impinging the metal [31]. Another very interesting possibility is to excite the surface plasmons in a small metallic particle, instead of in an infinite surface. This possibility is discussed in more detail in section 1.1.3, after we describe propagating plasmons in graphene.

1.1.2. Propagating surface plasmon polaritons in graphene

In recent years there has been a growing interest in the excitation of plasmons in graphene. Graphene is a conductive two-dimensional allotrope of carbon with atoms arranged in a hexagonal lattice, corresponding to a single layer of graphite. However, it exhibits different properties than bulk graphite due to its unique electronic band structure that resembles a semiconductor with zero energy gap [36] and linear electron dispersion relation. Since graphene has only a monoatomic thickness (around 3.4 Å), it can often be represented as a 2D material with zero thickness and described by its in-plane conductivity [37]

$$\sigma_{\text{gph}}(\omega) = \frac{e^2 E_{\text{F}}}{\pi \hbar^2} \frac{i}{\omega + i\tau^{-1}}, \quad (1.8)$$

where E_F is the Fermi level of graphene and $\tau = 1/\Gamma_{\text{gr}}$ is the relaxation time. Eq. 1.8 considers a simple description of σ_{gph} based on the Drude model, because in the infrared region where the SPPs are excited this term is the most important contribution.

We can describe the excitation of propagating SPPs in graphene in a similar way as in section 1.1.1. If the graphene is situated at the interface between media with generic dielectric constant ε_1 and ε_2 , the reflection coefficient for a plane wave incoming from the ε_1 media is [37]

$$r_p = \frac{\varepsilon_2 k_{1z} - \varepsilon_1 k_{2z} + \frac{\sigma_{\text{gph}}}{\varepsilon_0 \omega} k_{1z} k_{2z}}{\varepsilon_2 k_{1z} + \varepsilon_1 k_{2z} + \frac{\sigma_{\text{gph}}}{\varepsilon_0 \omega} k_{1z} k_{2z}}, \quad (1.9)$$

where k_{1z} and k_{2z} are the normal components of the wave vector in the surrounding media. Typically, propagating SPPs in graphene are characterized by a very large parallel wave vector component $q \gg k_i = \sqrt{\varepsilon_i} \omega / c$, so that we can then assume [37]

$$k_{iz} = \sqrt{\varepsilon_i \left(\frac{\omega}{c}\right)^2 - q^2} \simeq iq. \quad (1.10)$$

We can then derive the dispersion relation of propagating SPPs in graphene by finding the pole of the right hand side of Eq. 1.9

$$q = \frac{i(\varepsilon_1 + \varepsilon_2)\varepsilon_0 \omega}{\sigma_{\text{gph}}}. \quad (1.11)$$

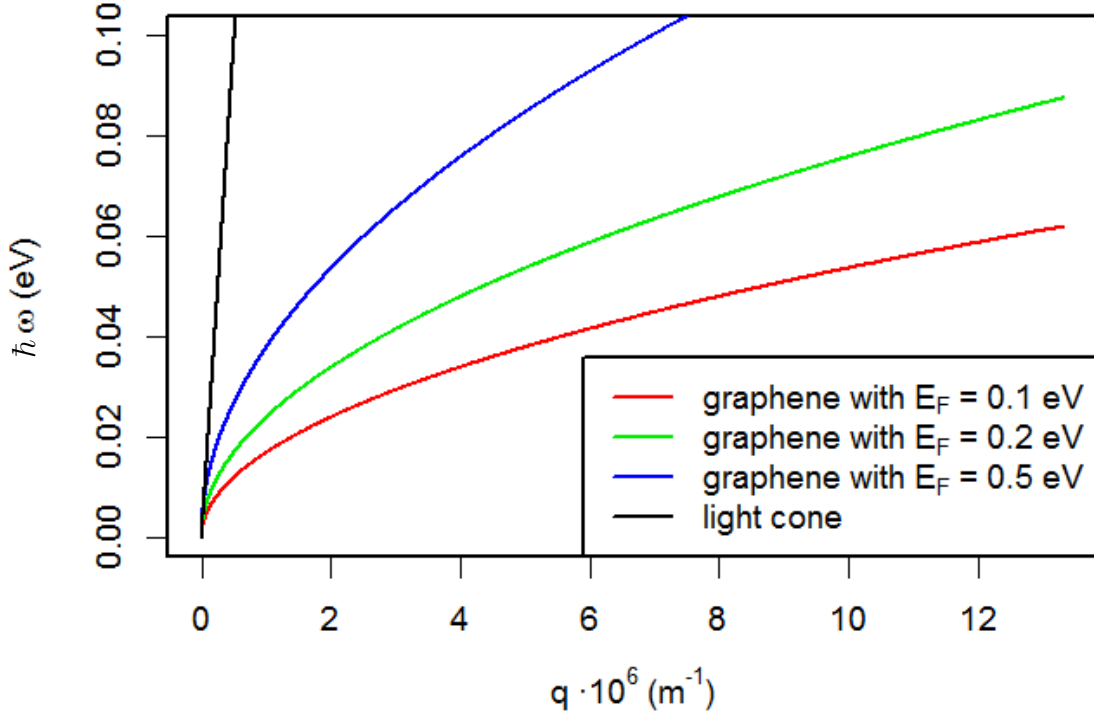


Figure 1.3: Dispersion relation of the surface plasmon polaritons in a graphene layer in vacuum ($\varepsilon_1 = \varepsilon_2 = 1$). The plotted data correspond to three different Fermi levels of graphene E_F . The black line corresponds to the light cone $q = \sqrt{\varepsilon_1} \omega / c$.

The dispersion relation is shown in Fig. 1.3, where for simplicity we specify the surrounding media as vacuum ($\varepsilon_1 = \varepsilon_2 = 1$), and use $\tau \approx 10^{-13}$ s (extracted from the experimental values for the charge carrier mobility [36, 38]) and $E_F = 0.1$ eV, 0.2 eV and 0.5 eV.

1.1. PLASMON POLARITONS

The dispersion relation of graphene is almost quadratic ($q \simeq \omega^2$ in the plotted mid and far-infrared region). By comparing the dispersion relation with the light cone we can see that for energies larger than about 20 meV the parallel wave vector component q of graphene is much larger than that of light ($q = \sqrt{\epsilon_1}\omega/c$), confirming the assumption used in Eq. 1.10. Eq. 1.10 also implies very large imaginary k_{iz} resulting in strong confinement in the z -direction.

A key advantage of SPPs in graphene when compared to those in metallic interfaces is the possibility to change the dispersion relation. The tunability is shown in Fig. 1.3 by the shift of the dispersion relation to higher energies with increasing Fermi energy E_F . Since the electron dispersion relation of graphene resembles a zero gap semiconductor, it is possible to effectively tune the Fermi energy by electrostatic doping, for example by applying a voltage or by an interaction of graphene with a material in its vicinity.

1.1.3. Localized surface plasmon polaritons in metallic particles

The propagating surface plasmon polaritons in infinite metallic or graphene flat surfaces confine the field only in one direction (normal to the surface). Full nanometric confinement in all three dimensions can be achieved by using finite structures, e.g. metallic particles (often called nanoantennas). The boundaries of a particle together with the metallic response generate discrete sets of localized modes of charge density oscillation at specific frequencies, which are strongly localized and thus are called localized surface plasmon polaritons (LSPP). These LSPPs can be directly excited by a laser beam.

To illustrate the properties of localized plasmons, we can derive the response of a metallic sphere with radius a and dielectric function ϵ_m located in a dielectric with ϵ_d . If the particle is small, we can solve this system analytically under the quasi-static approximation [4, 14]. In this approximation, the time derivatives in Maxwell's equations are assumed much smaller than the space derivatives and the field exciting the system can be taken as constant. In this case, the equation $\nabla \cdot \mathbf{E} = 0$ implies that the electric field can be expressed as a gradient of a potential $\mathbf{E} = -\nabla\Phi$, leading to the Laplace equation $\nabla^2\Phi = 0$. The solution of this equation inside and outside of the sphere (in spherical coordinates r and θ) is

$$\Phi_{\text{inside}} = -E_0 \frac{3\epsilon_d}{\epsilon_m + 2\epsilon_d} r \cos\theta, \quad (1.12)$$

$$\Phi_{\text{outside}} = -E_0 r \cos\theta + E_0 \frac{\epsilon_m - \epsilon_d}{\epsilon_m + 2\epsilon_d} a^3 \frac{\cos\theta}{r^2}, \quad (1.13)$$

where E_0 is the amplitude of the external field (oriented in the direction corresponding to $\theta = 0^\circ$).

Eqs. 1.12 and 1.13 were derived considering the solutions of the Laplace equation that are not infinite either far away or at the center of the particle, and that form an illuminating plane wave in region far away [4, 14]. The first part of the expression for the electric potential outside of the particle corresponds to the external excitation and the second part is the response of the particle, whose spatial variation is the same as for an electric dipole

$$\Phi_{\text{dipole}} = \frac{p}{4\pi\epsilon_0\epsilon_d} \frac{\cos\theta}{r^2}, \quad (1.14)$$

with p being the dipole moment. We thus see that the sphere behaves as a dipole with dipole moment

$$p = \varepsilon_d \alpha E_0 = 4\pi\varepsilon_0\varepsilon_d a^3 \frac{\varepsilon_m - \varepsilon_d}{\varepsilon_m + 2\varepsilon_d} E_0 , \quad (1.15)$$

where we define the polarizability α of the sphere as

$$\alpha = 4\pi\varepsilon_0 a^3 \frac{\varepsilon_m - \varepsilon_d}{\varepsilon_m + 2\varepsilon_d} . \quad (1.16)$$

The frequency of this dipolar mode can be derived by finding the pole of Eq. 1.16, i.e. when the metal permittivity fulfils $\varepsilon_m = -2\varepsilon_d$, which for the case of ε_d corresponding to vacuum and ε_m described by the lossless Drude model (Eq. 1.1) yields the result $\omega_{\text{dipole}} = \omega_p/\sqrt{3}$. The dipolar resonance can be detected experimentally by measuring the scattered and absorbed power, which corresponds to the scattering and absorption of a dipole of the strength given by Eq. 1.15 [28, 39]. The power is often normalized by the incoming intensity $I = 1/2 c\sqrt{\varepsilon\varepsilon_0} |E_0|^2$ giving the scattering and absorption cross-section

$$\sigma_{\text{scatt}} = \frac{k^4}{6\pi\varepsilon_0^2} |\alpha|^2 , \quad (1.17)$$

$$\sigma_{\text{abs}} = \frac{k}{\varepsilon_0} \text{Im}(\alpha) . \quad (1.18)$$

The spectral dependence of the scattering cross section of a gold sphere with radius $a = 15$ nm situated in vacuum, as given by Eq. 1.17, is shown in Fig. 1.4. Here, for ε_m we

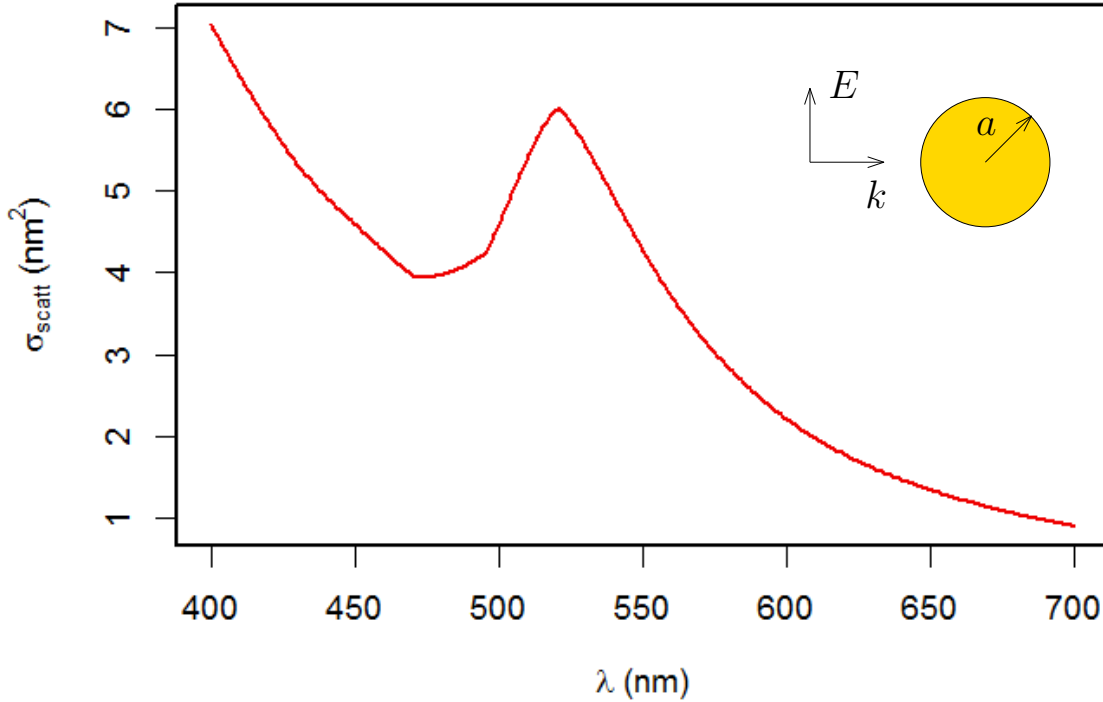


Figure 1.4: Scattering cross section of a gold sphere with radius $a = 15$ nm in vacuum. The plotted data are obtained from Eq. 1.17 using the quasi-static approximation.

1.1. PLASMON POLARITONS

use the experimentally measured values [30]. We note that Drude model is not appropriate here as it neglects interband transitions, which can affect the exact strength and position of the plasmonic resonances. The peak at 520 nm corresponds to the dipolar plasmonic resonance of the structure. The increase at 400 nm is associated with a general dependence $\sim 1/\lambda^4$ of the scattering cross section of small particles at non-resonant wavelengths (this dependence can be obtained by inserting a constant permittivity into Eq. 1.17).

In practice, it is often necessary to consider structures other than a sphere to tune the resonance to a desired frequency or to optimize the strength and confinement of the near fields. For example, two closely situated spheres (a sphere dimer) are often used, with the illumination light polarized along the axis joining them. The light excites the dipolar resonance at each sphere, which then couple via electromagnetic (Coulomb) interaction. For the parallel or antiparallel configuration of the dipole moments in the spheres we obtain the bonding (symmetric) and antibonding (antisymmetric) modes, respectively, which are analogous to bonding and antibonding hybridization states of interacting atomic orbitals. The antibonding mode has an energy higher than the single dipolar mode and can be excited by a beam of electrons passing through the gap, but not by light illumination because of the symmetry of the mode (charges symmetric with respect to the center of the gap, i.e. the antiparallel dipole moments cancel out).

Light couples with the bonding mode (of energy lower than the dipolar mode of a single sphere), which is characterized by a distribution of charges of opposite sign at both sides of the gap and thus by a strong enhancement of the field between the two spheres. As the

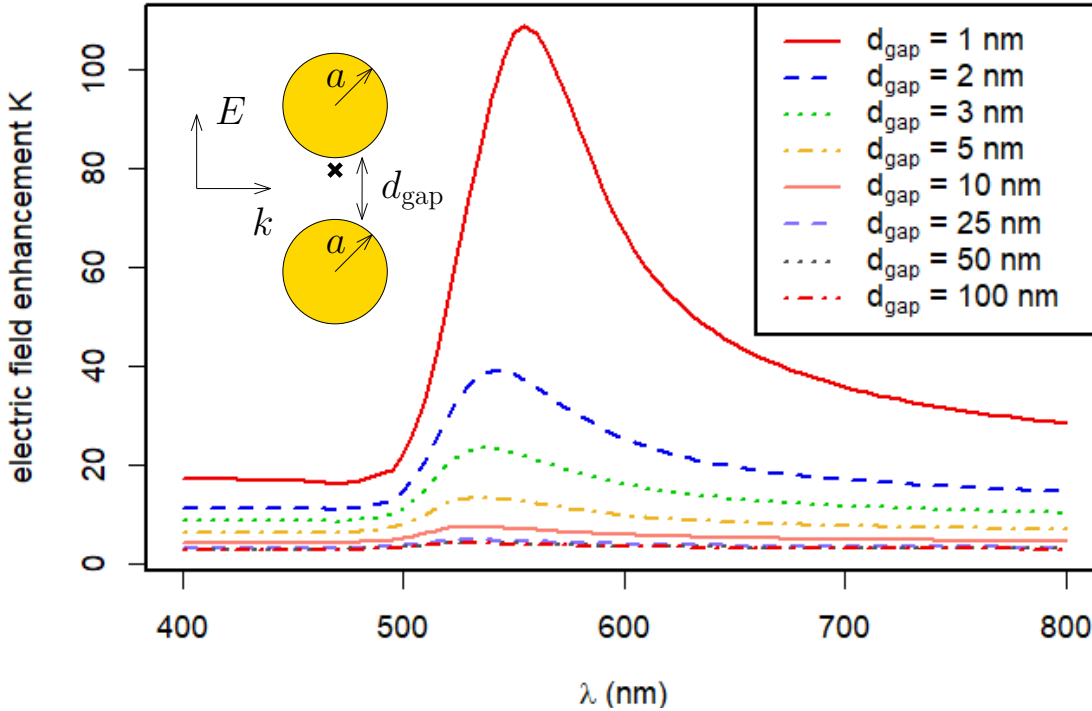


Figure 1.5: Field enhancement $K = |\mathbf{E}| / |\mathbf{E}_0|$ spectra of a gold sphere dimer as a function of the interparticle distance d_{gap} . The spheres have radius $a = 15$ nm, and are illuminated by light polarized along their common axis. The field enhancement is evaluated at a point on the common axis between the spheres 0.5 nm away from one of them (marked by the cross).

particles are brought closer together, they interact more strongly, leading to larger fields at the gap and to a redshift of the resonance frequency (corresponding to the lower energy of the mode). This behaviour is illustrated in Fig. 1.5, which represents the enhancement of the field $K = |\mathbf{E}| / |\mathbf{E}_0|$ in between two gold spheres (ϵ_m from [30]) of 15 nm radius at a distance of 0.5 nm from a sphere on the axis joining the two spheres. The calculations were performed using the finite element method (see chapter 3 for details). Our calculations indicate that the field enhancement can reach values larger than 100 for 1 nm gap distance (contrary to the enhancement of 4-5 for a large separation corresponding to individual isolated spheres), and that the resonant peak (corresponding to the dipolar mode) shifts from around 520 nm for large separation distance to about 560 nm for 1 nm gap.

1.2. Raman spectroscopy

Raman spectroscopy is a widespread technique used for characterization of molecules and materials [1, 2]. In most cases, when a light photon of frequency ω interacts with a molecule, it is scattered elastically (Rayleigh scattering), i.e. the frequency is unchanged. However, the photons can also interact inelastically with the molecule (through so called Raman scattering), exchanging energy with the i -th rotational or vibrational mode of the molecule with typical energy $\hbar\Omega_i \approx 100$ meV in the mid-infrared region. The coupling leads to the excitation of a virtual state and subsequent emission of a photon with different energy (Fig. 1.6). If a vibrational or rotational state with energy $\hbar\Omega_i$ has been excited in the molecule, the emitted photon has lower energy $\hbar\omega - \hbar\Omega_i$ (resulting in a so called

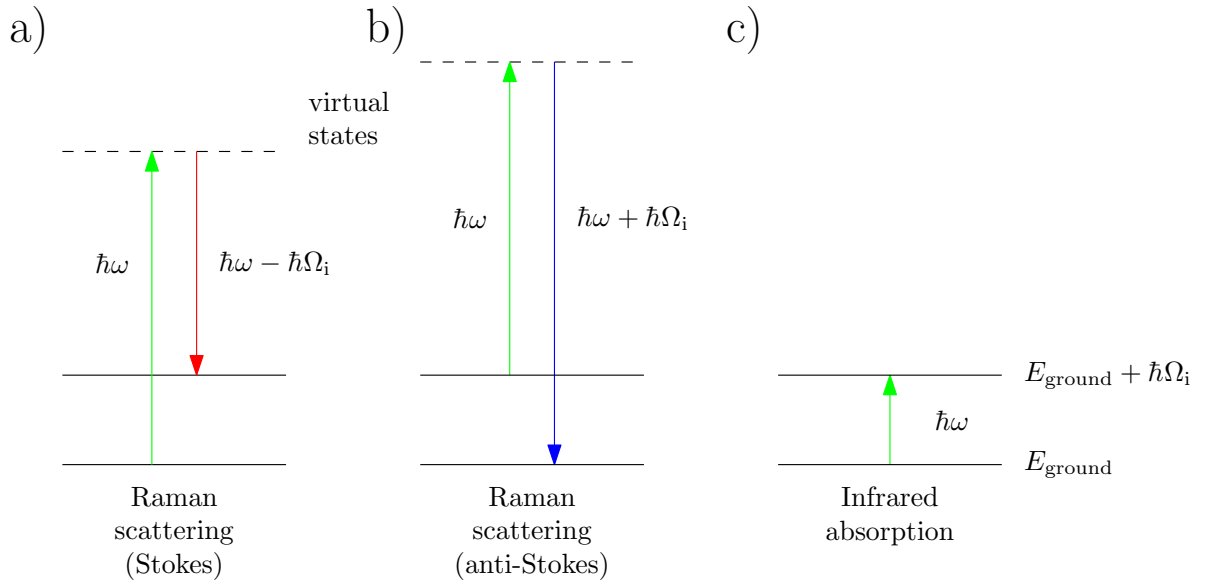


Figure 1.6: Transitions between energy levels of a molecule for Raman scattering and infrared absorption. (a,b) In Raman scattering the energy of photons $\hbar\omega$ is changed by a value $\hbar\Omega_i$ of an i -th mode of vibration. The process when a photon loses energy by exciting the molecule gives rise to a Stokes peak in the measured spectrum (a). The opposite case occurs when an excited molecule transfers part of its energy to a photon resulting in an anti-Stokes peak (b). (c) In infrared absorption photons of energy $\hbar\Omega_i$ are directly absorbed, resulting in the transition between vibrational energy levels. The energy E_{ground} corresponds to the ground vibrational energy level of the molecule.

1.2. RAMAN SPECTROSCOPY

Stokes peak in the spectra, Fig. 1.6a). It is also possible that the molecule is already in an excited vibrational state and after the interaction with the incident light a photon of higher energy $\hbar\omega + \hbar\Omega_i$ is emitted (giving rise to the anti-Stokes peak in the spectrum, Fig. 1.6b).

Every molecule has a specific set of vibrational and rotational modes that results in characteristic Stokes and anti-Stokes peaks (a molecular fingerprint) which is very useful for chemical analysis. However, due to the small cross section of the scattering (weak interaction of molecules with light) it is hard to inspect low concentrations of molecules. As we discuss in the next subsection, the signal can be enhanced by coupling the molecules with SPPs.

1.2.1. Surface-enhanced and tip-enhanced Raman spectroscopy

In the search for a method capable of enhancing the signal in Raman spectroscopy, it was found that when a molecule is placed on a rough metallic substrate the Raman signal is amplified. This method is therefore called surface-enhanced Raman spectroscopy (SERS) [5, 6, 7]. The enhancement of the signal is caused by the excitation of SPPs at regions between bumps or sharp features in the rough surface that can localize the electromagnetic energy and thus lead to a strong interaction with the molecules. Additionally, a chemical mechanism due to electron transfer between the molecules and the substrate or similar processes [10] also contribute to the enhancement. Moreover, the plasmonic enhancement can be controlled by designing specific metallic nanoantennas that support optimized plasmonic resonances. These nanoantennas often exploit small gaps between two particles due to the large field enhancement at the gap that we discussed in section 1.1.3.

A particular configuration that relies on the field enhancement at such nanogaps uses a sharp metallic tip which acts like a metallic nanoantenna that amplifies and confines the electromagnetic energy at the gap between the tip apex and the underlying metallic substrate. In this case, we often talk about tip-enhanced Raman spectroscopy (TERS) [11]. Furthermore, by moving the tip over the substrate it is possible to map the response of the samples with a resolution that is set by the confinement of the plasmonic field, and thus can go far beyond the diffraction limit [11, 40].

1.2.2. Graphene-enhanced Raman spectroscopy

In recent years the possibility of using graphene to enhance the Raman signal has been discovered, yielding a technique called graphene-enhanced Raman spectroscopy (GERS) [12]. However, since the SPPs of graphene are located in the THz and infrared region [41, 42], at much lower energies than the incident laser used in these experiments, the main mechanism of the enhancement caused by graphene is likely based on the direct chemical interaction of graphene with molecules under study, mainly through the overlap of their electronic structures and charge transfer. The enhancement caused by this chemical mechanism is selective to the molecules under investigation, enhancing mainly molecules with a geometric structure similar to that of graphene (symmetry group D_{6h}) and with optimal energies of the highest occupied molecular orbital (HOMO) and the lowest unoccupied molecular orbital (LUMO) with respect to the Fermi energy E_F of graphene and the energies of the photons $\hbar\omega$ and the phonons $\hbar\Omega_i$. The highest enhancement oc-

curs when the difference in these energies match, i.e. either i) $\hbar\omega = \text{LUMO} - \text{HOMO}$ or $\hbar\omega = \text{LUMO} - \text{HOMO} \pm \hbar\Omega_i$, ii) $E_F = \text{LUMO} \pm \hbar\Omega_i$ or $E_F = \text{HOMO} \pm \hbar\Omega_i$, iii) $\hbar\omega = E_F - \text{HOMO}$ or $\hbar\omega = E_F - \text{HOMO} \pm \hbar\Omega_i$, or iv) $\hbar\omega = \text{LUMO} - E_F$ or $\hbar\omega = \text{LUMO} - E_F \pm \hbar\Omega_i$ [43, 13].

1.3. Surface-enhanced infrared absorption spectroscopy

The infrared absorption spectroscopy (IRA) [3] is based on the direct absorption of light due to the excitation of the vibrational states of molecules, as is depicted in Fig. 1.6c. In this case, the photons have an energy $\hbar\omega$ identical with the energy $\hbar\Omega_i$ of the molecular vibration transitions. The absorption can then be monitored by measuring the intensity of light that is transmitted or reflected (reflected from the substrate, i.e. transmitted twice through the molecules) as a function of ω . Similar to SERS, IRA can be enhanced by situating the molecule near a metallic structure supporting plasmonic resonances, giving rise to surface-enhanced infrared absorption spectroscopy (SEIRA) [9, 8]. The resonance peaks in the SEIRA spectra are the result of the coherent interaction between the SPPs and molecular vibrational states, so that instead of simple Lorentzian lines the measurements often reveal more complex spectral features (Fano lines) that are the result of adding a complex-valued Lorentzian (describing the fields scattered by the molecule) to a slowly varying plasmonic background. The Fano lines contain the chemical information on the molecular vibrations and their strength can be generally increased by optimizing the plasmon resonances to induce strong enhancement of the local intensity at the position of the molecule.

1.4. Scanning near-field optical microscopy

In studies concerned with the optical imaging of micro and nanostructures (or positions of quantum nanodots, or even individual molecules) the key factor is the achievable spatial resolution, which depends on the employed technique, most notably whether only far-field (i.e. propagating light waves) or also near-field (i.e. fields containing also evanescent waves) is used [14]. In conventional optical microscopes, which are both illuminating the sample and detecting the signal in the far-field, the maximum resolution is given by the diffraction limit of light which can be expressed by the Rayleigh criterion

$$\Delta x = 0.61 \frac{\lambda}{\text{NA}}, \quad (1.19)$$

where Δx is the minimum spotsize, λ is the wavelength of light and $\text{NA} = n \sin\theta$ is the numerical aperture of the objective (n being an index of refraction of a surrounding medium and θ being a half-angle of the light cone exiting the objective). For example, for green light ($\lambda = 500 \text{ nm}$) and for $n = 1.4$, the minimum spotsize reaches 220 nm, which in some cases is much more than the size of studied objects.

Scanning near-field optical microscopy (SNOM) is capable of overcoming the diffraction limit by utilizing the interaction of the near-field (scattered from sharp features or caused by surface plasmons) with a sharp tip [4, 14, 15]. The tip is scanned over the

1.4. SCANNING NEAR-FIELD OPTICAL MICROSCOPY

sample in a constant distance from the sample ranging between 1 and 100 nm, acting as a source or a detector of the near-field. In most cases the tip is fabricated from a glass fiber etched into a sharp cone with a metallic coating and a subwavelength aperture in the coating at the end, through which the light cannot pass directly due to the diffraction limit, but rather the near-field in the vicinity of the aperture is coupled with the propagating modes in the fiber (which in turn significantly decreases the intensity). However, bare fiber tips (with lower attenuation of signal, but also worse resolution due to lower confinement) or apertureless tips find their applications, too. The tip is mounted on a tuning fork which enables the control of a constant distance of the tip from the sample by a shear-force feedback: the tuning fork with the tip attached is kept vibrating at its resonant frequency, and when the tip approaches the sample, it starts to interact with the sample (experience shear forces) and changes the amplitude and frequency of the resonant vibration [15].

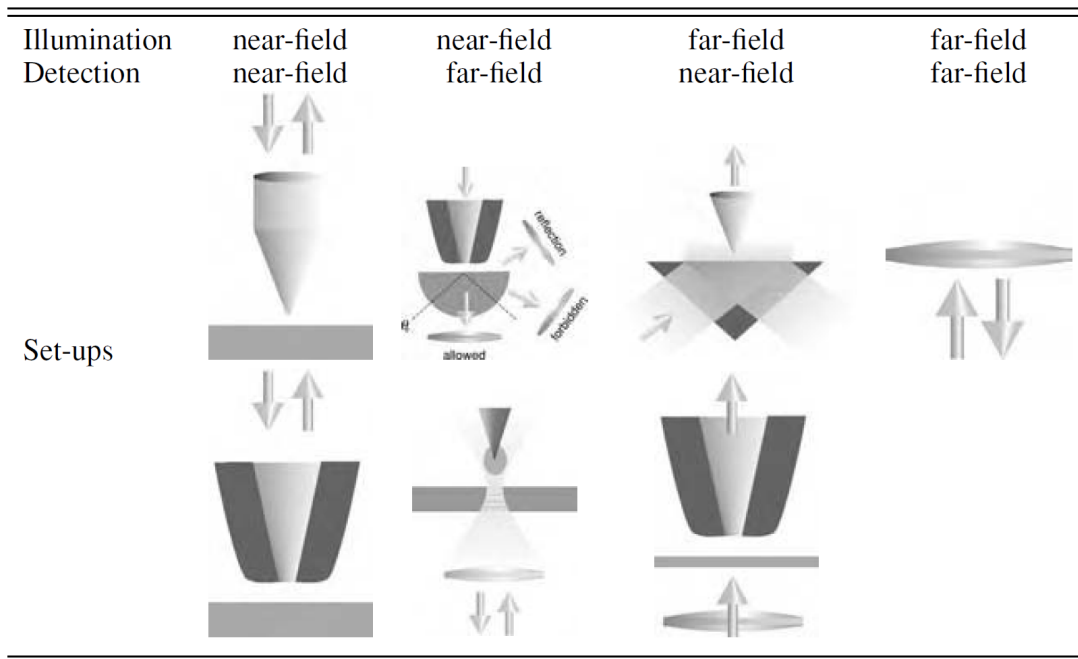


Figure 1.7: Overview of different scanning near-field optical microscope configurations varying in the form of the near-field or far-field illumination and detection (conventional optical microscopy is mentioned in the last column). Adopted from [14]

The three configurations of SNOM with either the illumination or detection (or both) in the near-field are depicted in Fig. 1.7 (along with the far-field optical microscopy). In the most commonly used configuration the tip is used as a source of the near-field illumination, causing the studied structures to interact with the near-field confined beneath the tip and scattering the light into the far-field, which is subsequently collected (in reflection or transmission) via an objective and brought to a detector. Instead of the metal coated glass fiber tip it is possible to use an STM (scanning tunneling microscope) tip that behaves like a scatterer of the far-field illumination and thus provides a near-field source, creating the so called scattering SNOM (s-SNOM). This technique is used e.g. for imaging fluorescent molecules [19] or quantum dots [20]. The experimental set up can also be inverted, using the far-field as illumination source and then scanning with the tip to pick up the signal of the near-field above the sample. Finally, one can employ both

the near-field illumination and detection, further enabling the near-field confinement and control of the imaging (at the expense of signal reduction by light passing through an aperture twice), by using either the same tip for the illumination and detection (with a beamsplitter in the optical path) or two different tips [44]. The incoming near-field can also take the form of surface plasmons, which are excited at gratings or slits in a metal layer illuminated from the back side by a laser (see Fig. 1.8), and then the tip is used for mapping the propagation of SPPs [18, 17].

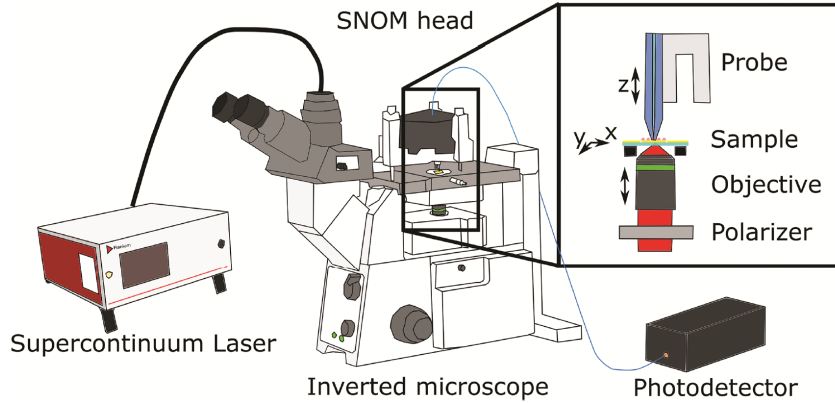


Figure 1.8: Scheme of a scanning optical microscope with a tip used for detection of the near-field. The far-field illumination is achieved in an inverted optical microscope, where a laser beam is focused by an objective onto the back side of the sample. The light subsequently either interacts with molecules or other structures on top of a transparent substrate, or excites surface plasmon polaritons on a metal substrate through slits. Adopted from [24]

1.4.1. Sensitivity of SNOM tips to components of electromagnetic field

When using a SNOM tip in the collection mode, i.e. the tip serves the role of a detector, it is important to consider the sensitivity of the tip to different components of the electromagnetic field, since this directly affects what the measured signal images show. Most works claim that the SNOM probes with an aperture measure the in-plane component of the electric field (perpendicular to the tip axis in experiments with a tip scanned over a planar sample) [21, 22, 23], which seems reasonable, because this orientation of the vector of the electric field is the same as for propagating modes in the fiber.

Nonetheless, this explanation holds only for cases when the diameter of the aperture is large enough for the light to pass through, and the situation where tips with small apertures or even without apertures are used might differ. In fact, it has been shown that when an apertureless metal coated glass fiber tip is used, it is sensitive to both transversal and longitudinal waves, which couple respectively to linearly and radially polarized modes in the fiber by the process of the field tunneling through the metal coating [45]. The case of a tip without an aperture being sensitive to the out-of-plane component of the electric field (parallel to the tip axis) can be understood by an analogy with a scattering SNOM tips that are primarily sensitive to the out-of-plane component [16].

Interestingly, there are also studies in which it is claimed that rather the out-of-plane component is detected using a standard SNOM tip with an aperture [18, 24, 25]. The

1.4. SCANNING NEAR-FIELD OPTICAL MICROSCOPY

explanation of this phenomenon might be that the sensitivity to specific field components changes continuously with the change in the aperture diameter, and when this is combined with a field distribution under study with the out-of-plane component being prominent, then the detected signal might show higher intensity for the out-of-plane component [25]. Apart from the sensitivity to the different components of the electric field, certain tip geometries are also reported to probe the magnetic field [46, 47, 48].

Nevertheless, the exact mechanism by which the SNOM tip detects the electromagnetic field is still not completely understood, because the performed calculations so far used only very simplified models representing the tip as a cone with a finite height (rarely exceeding length of 1 μm) and monitoring the passing power only at selected positions.

2. Model

2.1. Model for tip-enhanced Raman and infrared absorption spectroscopy calculations

In the electromagnetic simulations of tip-enhanced spectroscopy we consider the situation shown in Fig. 2.1, which models the experiments performed by our collaborators at HU Berlin and ETH Zurich. In essence, an illuminated sharp tip is used to excite a monolayer of molecules deposited over a substrate. The tip is modelled as a cone with apex angle $2\alpha = 24^\circ$, height $h = 500$ nm and a rounded apex with radius $R = 15$ nm. The material of the tip is silver characterized by a dielectric function taken from Johnson and Christy [30]. For the SEIRA experiment, where the illumination wavelength is in the infrared, we extrapolate the experimental values of the visible range by considering that the value of the dielectric function can be fit in this infrared range as a sum of a constant (representing the d-electron contribution) and a Drude term [29, 30] (Eq. 1.1). The substrate is a 200 nm thick layer of gold, sufficiently thick to behave as a semi-infinite substrate. The dielectric function of gold is also taken from Johnson and Christy [30] and, for the SEIRA simulations, it is extrapolated towards high wavelengths in the same manner as for silver. On top of the substrate there is a dielectric layer representing a self-assembled monolayer (SAM) of oligomeric phenylene ethynylene thiol (OPE). In the calculations we simulate the molecular layer as a homogeneous dielectric layer with a

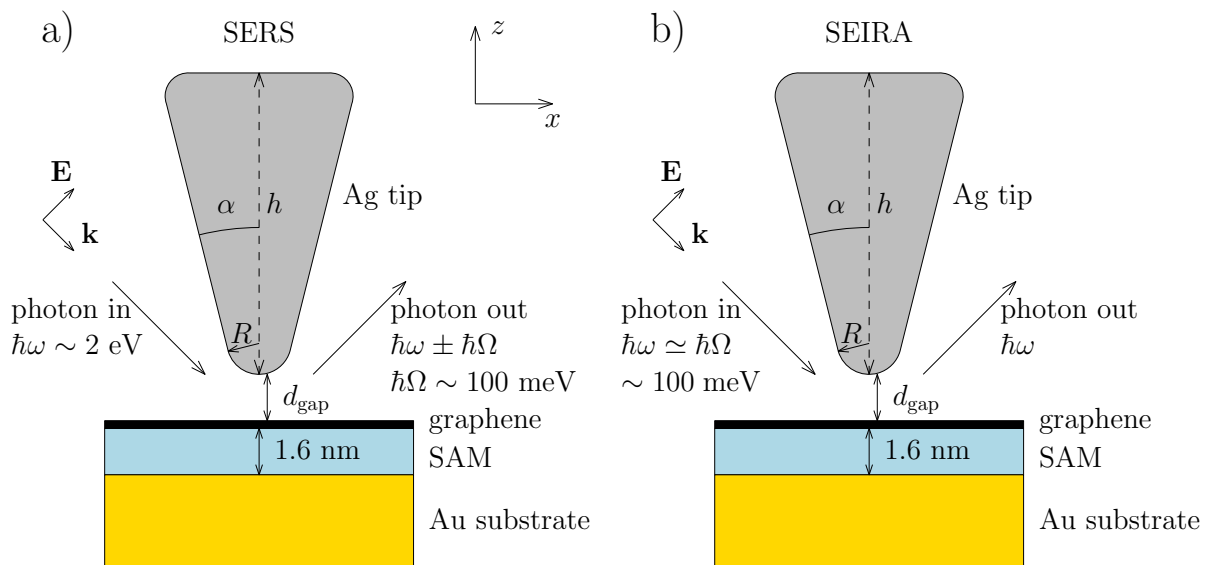


Figure 2.1: Scheme of the model geometry used for SERS and SEIRA calculations. The geometry consists of a $h = 500$ nm long silver tip with an apex radius $R = 15$ nm and apex angle $2\alpha = 24^\circ$, situated over a gold substrate that is covered by a 1.6 nm thick molecular layer. Graphene can be also deposited over the molecules. The tip is situated in air and the gap distance between its apex and the molecular layer (or graphene) is d_{gap} . The illumination energy is $\hbar\omega$ and the molecules present a vibrational mode at $\hbar\Omega$. In SERS experiments the sample is illuminated by visible light of energy $\hbar\omega$ and the signal is measured at energy $\hbar\omega \pm \hbar\Omega$ (Stokes or anti-Stokes photons). The SEIRA experiments are based on the absorption of infrared light with energy $\hbar\omega \simeq \hbar\Omega$.

thickness 1.6 nm [49] and a real refractive index 2.25 [50]. The molecules can be covered by a layer of graphene, which we characterize by means of its surface conductivity $\sigma_{\text{gph}}(\omega)$ on the top surface of the layer of molecules using the expression [37]

$$\sigma_{\text{gph}}(\omega) = \frac{e^2 E_{\text{F}}}{\pi \hbar^2} \frac{i}{\omega + i\tau^{-1}} + \frac{e^2}{4\hbar} \left[U(\hbar\omega - 2E_{\text{F}}) + \frac{i}{\pi} \log \left| \frac{\hbar\omega - 2E_{\text{F}}}{\hbar\omega + 2E_{\text{F}}} \right| \right], \quad (2.1)$$

where E_{F} is the Fermi level of graphene, τ is the relaxation time of graphene, set as $\tau \approx 10^{-13}$, ω is the angular frequency of light, e is the electron charge and U is the Heaviside step function. This equation was derived assuming zero temperature. We note that we use more complex expression than in the introduction (Eq. 1.8) to take into account interband transitions in graphene, which can significantly affect the response for energies $\hbar\omega > 2E_{\text{F}}$.

The medium above the sample is air with an optical index $n = 1$. The whole geometry is then illuminated by an electromagnetic plane wave coming from the air side, with angle of incidence $\theta_i = 30^\circ$ relative to the surface normal and with amplitude $|\mathbf{E}_0|$. Finally, we choose the coordinate axes so that the z axis is parallel to the tip axis (and surface normal) and the x axis is parallel to the surface plane, with xz the plane of incidence that contains the incident wave vector. Position $z = 0$, $x = 0$ corresponds to the point at the air-molecules interface beneath the tip apex.

For SERS and TERS experiments (Fig. 2.1a), the signal of interest is dependent on the field enhancement in the layer of molecules $K(\omega) = |\mathbf{E}(\omega)| / |\mathbf{E}_0|$, where $|\mathbf{E}(\omega)|$ is the amplitude of the total electric field. We consider the case of sufficiently low intensity [51], where the population of phonons (molecular vibrations) is thermal (i.e. unaffected by the laser). The SERS enhancement signal is then given by two factors: first, the local enhancement of the incoming light intensity $K^2(\omega)$, and second, the enhancement of the emission rate of the molecules at frequencies $\omega \pm \Omega$. The latter is proportional to the intensity enhancement at the emission frequencies $K^2(\omega \pm \Omega)$ due to reciprocity [52]. The SERS enhancement is thus $K^2(\omega)K^2(\omega \pm \Omega)$. We use the approximation $K^2(\omega) \simeq K^2(\omega \pm \Omega)$, which is often valid because the plasmonic resonances are relatively wide in comparison to the frequency difference Ω of the incoming and outgoing light. As a consequence, we obtain the SERS/TERS enhancement in the following as K^4 .

To estimate the effect of graphene on the SEIRA signal, we also perform calculations in the infrared region (Fig. 2.1b). As we discussed in section 1.3, the SEIRA signal in experiments can exhibit complex interference features. For simplicity, the value of K^2 can be considered to represent the enhancement of the absorption of the molecule.

2.2. Model for scanning near-field optical microscope calculations

For the simulations of scanning near-field optical microscope we use a model shown in Fig. 2.2 based on the geometry proposed by our collaborators at Institute of Physical Engineering at BUT in Ref. [24] with some modifications applied. In principle the model reflects the experimental set-up of an inverted optical microscope with a SNOM probe in the collection regime (see Fig. 1.8), where the illumination is provided by a slightly defocused laser beam (so that the illumination is practically homogeneous over the studied region) from the back side of the sample composed of a glass substrate with a gold layer

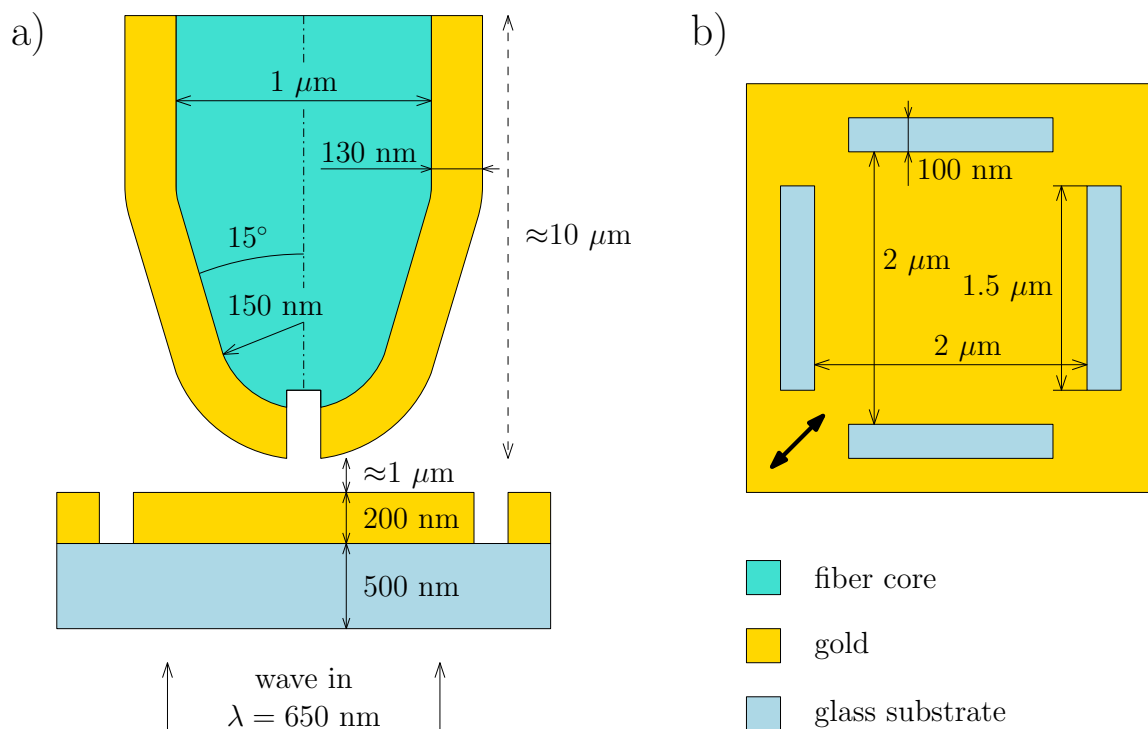


Figure 2.2: Scheme of the model geometry used for SNOM calculations. The whole model (side view in (a)) is composed of a glass substrate with a gold layer on top in which a square pattern of four slits is made (top view in (b)). A SNOM tip (consisting of a conical and a cylindrical part) with a glass core and a metallic coating (in which an aperture is created) is located above the sample. The geometry is illuminated from the side of glass substrate with light linearly polarized along the diagonal of the slit square pattern (depicted as a bold double arrow in (b)).

on top with slits etched through arranged in a square pattern; subsequently the laser excites a standing SPP wave on the top side of the gold layer through the slits, which is then measured with a SNOM tip with a glass fiber core and a metallic coating with an aperture at the apex (milled with a focused ion beam).

In our calculations the sample consists of a 500 nm high layer of glass with a index of refraction $n = 1.5$ and a 200 nm high layer of gold with a dielectric function taken from Johnson and Christy [30]. In the gold layer a square pattern of four slits through the height of the layer is created (Fig. 2.2b): the area inside of this pattern has the form of a square with dimensions $2 \mu\text{m} \times 2 \mu\text{m}$, the width of the slits is 100 nm and their length is $1.5 \mu\text{m}$, so that the slits don't meet in corners; this corresponds to the experimental configuration, where it is necessary for the inner gold square to be connected to the rest of the layer (to prevent charging).

Above the sample a SNOM tip is located, which consists of a glass fiber core and metallic coating. The glass fiber core with an optical index $n = 1.4$ has a conical geometry at the end near the sample with an apex angle $2\alpha = 30^\circ$ and a rounded apex with radius $R = 150 \text{ nm}$, the cone becomes wider further away from the sample, until it reaches a diameter of $1 \mu\text{m}$ (at height of around $1.4 \mu\text{m}$) where the fiber becomes cylindrical; the total height of the core is slightly lower than $10 \mu\text{m}$ (the total height of the simulation domain above the sample is exactly $10 \mu\text{m}$). The fiber is coated with a metallic layer of

2.2. MODEL FOR SCANNING NEAR-FIELD OPTICAL MICROSCOPE CALCULATIONS

a uniform thickness of 130 nm; the metal used is either gold (with a dielectric function taken from Johnson and Christy [30]) or aluminium (with a dielectric function taken from Rakić [53]). A cylindrical aperture with a varying diameter ($d = 60 - 160$ nm) is created at the apex, boring through the coating and partially into the core (total height of the side of the aperture cylinder is 200 nm). The tip is positioned above the sample in a height that would correspond to a gap $d_{\text{gap}} = 1$ nm between the sample and the coating without an aperture, the presence of the aperture increases the gap, however, this solution is chosen so that the position of the tip doesn't change when a different aperture diameter is used. The rest of the model (the area around the tip, slits in gold layer and the tip aperture) is filled with air, i.e. with a material with an index of refraction $n = 1$. The entire geometry is illuminated from bottom (i.e. from the glass substrate) with linearly polarized light (along the square pattern diagonal) with a free-space wavelength $\lambda = 650$ nm.

The signal measured in SNOM experiments is approximated in our simulations as the total radiant power (radiant flux) going through the core (cross-section of the core) given by equation

$$\Phi_e = \iint_A \mathbf{S} \cdot \mathbf{n} dA , \quad (2.2)$$

where \mathbf{S} is the Poynting vector, A is the fiber core cross-section area and \mathbf{n} is its normal vector.

3. Methods

3.1. Introduction to the finite element method

In order to solve the partial differential equations (PDE) describing the electromagnetic fields in our model, we use numerical calculations based on the finite element method (FEM) [54]. The FEM uses the weak formulation of the PDE, according to which the original PDEs are integrated over the domain volume. To evaluate the resulting equations, the FEM divides the space under study into a mesh of volume segments. The next step is to find the solution of the PDE in the form

$$\psi = \sum_i u_i \psi_i , \quad (3.1)$$

where ψ_i is a set of base functions and u_i are the variables to be obtained. In our case the base functions are the electric fields. The base functions are implemented in such a way that for each point in the mesh there is a base function ψ_i with a non-zero value in mesh elements around this point and a zero value elsewhere. As a consequence, when performing the integral in each volume element we only need to consider the overlap of very few base functions. The matrix describing the resulting set of linear equations (with u_i as the variables or unknowns) is thus sparse. Because the discretization in time can be rather computationally expensive, FEM often works in the frequency domain, where the time derivative is transformed according to $\partial/\partial t(f(t)) \rightarrow -i\omega f(\omega)$. A more detailed explanation can be found in [54].

One of the advantages of FEM is the ability to create a mesh that is finer near the tip-substrate gap (the region where the characteristic dimensions are smaller and where we want to obtain an accurate representation of the distribution of the fields), and coarser at other regions with larger features. This flexibility makes it easier to perform the multiscale simulations in Fig. 2.1, that include tips and substrates hundreds of nanometers long and at the same time features (such as the gap) down to 1 nm.

In particular, we use the program COMSOL Multiphysics [55], which is capable of solving various problems in physics and engineering, such as fluid and heat transfer analysis. Notably, it is possible to combine different phenomena, and for example calculate the optical fields induced by a laser and then how the absorbed electromagnetic energy translates into a change of temperature [56]. Our COMSOL calculations use the frequency domain approach implemented with the radio-frequency (RF) module, which is suitable for electromagnetic calculations in geometries with dimensions comparable with the wavelength of light. In this module the solution of the fields is found by solving the equation

$$\nabla \times \mu_r^{-1} (\nabla \times \mathbf{E}) - k_0^2 \left(\varepsilon_r + \frac{i\sigma}{\omega\varepsilon_0} \right) \mathbf{E} = 0 , \quad (3.2)$$

that fulfils Maxwell's boundary equations. \mathbf{E} is the electric field, ω is the angular frequency of light, $k_0 = \omega/c$ is the free-space wave vector and μ_r , ε_r and σ are the permeability, permittivity and conductivity, respectively, of the material being considered. Eq. 3.2 can be derived directly from the Maxwell's equations in frequency domain $\nabla \times \mathbf{E} = -i\omega\mathbf{B}$ and $\nabla \times \mathbf{H} = \mathbf{J}_f - i\omega\mathbf{D}$, by dividing the first equation by μ_r , applying an additional

3.1. INTRODUCTION TO THE FINITE ELEMENT METHOD

rotation and then substituting the second term by the second equation to eliminate the magnetic induction \mathbf{B} . $\mathbf{D} = \varepsilon_r \varepsilon_0 \mathbf{E}$ is the electric displacement field, $\mathbf{H} = \mathbf{B}/(\mu_r \mu_0)$ is the magnetic field and $\mathbf{J}_f = \sigma \mathbf{E}$ is the free current density. In our case we assume materials with no magnetic response, i.e. $\mu_r = 1$, and we include the conductivity in the complex permittivity ($\varepsilon_r + i\sigma/\omega\varepsilon_0 \rightarrow \varepsilon'_r$), thus setting $\sigma = 0$. In tip-enhanced spectroscopy simulations the graphene layer is implemented as a surface current density $\mathbf{J} = \sigma_{\text{gph}} \mathbf{E}_{\parallel}$ (considering only the electric field component parallel with the surface), so that it is an ideal 2D layer, i.e. with no thickness. σ_{gph} corresponds to the conductivity given by Eq. 2.1.

To obtain the optical response of the geometry of the tip-enhanced spectroscopy model discussed in section 2.1, we proceed in two steps. We first obtain the solution for the multilayer Au-SAM or Au-SAM-graphene system (without the tip). The stack is placed in a rectangular 3D simulation domain of dimensions $500 \text{ nm} \times 500 \text{ nm} \times 900 \text{ nm}$ (width \times depth \times height), and the field distribution can be obtained by applying Floquet periodic boundary conditions, under a plane wave excitation. As a second step we use the calculated field as a background field for the full tip-substrate system (Fig. 2.1). In this step, we use perfectly matched layers (PMLs) around the whole simulation domain to prevent undesired reflection of an outgoing wave (scattered from the tip) back inside the calculation domain. In the PMLs the space derivatives in the wave equation are transformed as $dx \rightarrow dx(1 + i\gamma(x)/\omega)$, where $\gamma(x)$ is a function chosen to avoid significant reflection at the simulation domain-PML interface and to attenuate efficiently the scattered radiation inside the PML. We note that in the first step with no tip we use Floquet periodic boundary conditions instead of PMLs because the latter are not perfect for a multilayer system, therefore, when applicable, the former are more adequate. On the other hand, we apply the PMLs once the tip is introduced because the use of Floquet conditions would be equivalent to introducing a periodic array of tips instead of a single one.

For the scanning near-field optical microscope simulations we use only a one-step calculation, since there is no reason to simulate the geometry without a tip (because the arrangement of slits has to be aperiodical as well) or without a tip and slits (because we would only get a reflection of the incoming wave, which, furthermore, comes in the perpendicular direction). The entire simulation domain of dimensions $2.44 \mu\text{m} \times 2.44 \mu\text{m} \times 10.7 \mu\text{m}$ (width \times depth \times height) is enclosed in PML, except for the bottom boundary, where the illuminating plane wave enters the geometry. It is also worth noting that the top end of the tip is in direct contact with the PML, which ensures that the tip is treated as infinite; this approach is possible (contrary to tip-enhanced spectroscopy simulations, where only a finite tip is used) due to illumination coming from the opposite side of the simulation domain.

In order to check that the obtained results are correct, we performed several convergence tests of our models: we varied the dimensions and meshing of the simulation domain, as also of the surrounding PMLs. These changes affected the results only weakly. Furthermore, we describe in the next sections how we also verified the numerical results against analytical solutions for simple systems. In particular, we choose two systems that are important components of the full tip-enhanced spectroscopy simulation model described in section 2.1. First, we consider a single sphere as a representative case of localized plasmonic resonances. Then, we compared the distribution of electric field in a multilayer system corresponding to the substrate in spectroscopic simulations in Fig. 2.1.

3.2. Comparing numerical and analytical results: gold sphere

The first system to check the calculations is a small gold nanosphere, which has a known analytical solution of the scattering cross-section discussed in section 1.1.3. As before, we consider a gold sphere with a radius $a = 15$ nm and permittivity taken from [30], surrounded by vacuum (a 400 nm thick layer in our calculation). The whole model was enclosed in a perfectly matched layer (PML) of a 250 nm thickness.

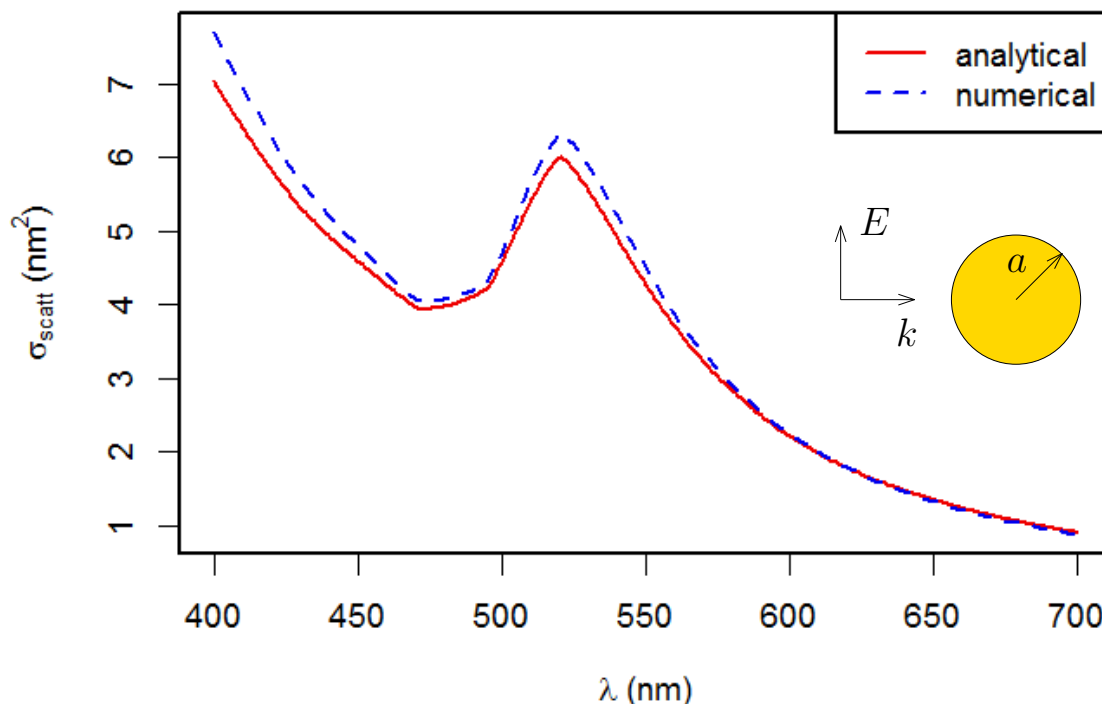


Figure 3.1: Scattering cross section of a gold sphere with radius $a = 15$ nm in vacuum. The values of the analytical quasi-static expression (Eq. 1.17, red solid line) are compared with the numerically calculated spectra (blue dashed line).

For this calculations, we are interested in the scattering cross-section of the sphere, which can be calculated as

$$\sigma_{\text{scatt}} = \frac{\oint_A \langle \mathbf{S}_{\text{scatt}} \rangle \cdot \mathbf{e}_r dA}{I_i}, \quad (3.3)$$

where $\langle \mathbf{S}_{\text{scatt}} \rangle$ is the Poynting vector of the scattered light, A is the closed spherical surface around the sphere over which the integration is done, \mathbf{e}_r is the unit vector normal to the surface A and I_i is the intensity of the incoming light. We compare in Fig. 3.1 the spectra of the analytical solution (solid red line, obtained from Eq. 1.17) with the results calculated in COMSOL (blue dashed line). We can see that the numerical results reproduce very satisfactorily the dipolar resonance obtained from the analytical solution.

3.3. Comparing numerical and analytical results: multilayer system

As a second test, we also implemented in the software RStudio an analytical model that gives the electric fields induced in multilayer systems. We use the transfer-matrix method [57] to relate the reflection and transmission coefficients of an interface and to describe the propagation through a medium. The details of this method are given in appendix A.

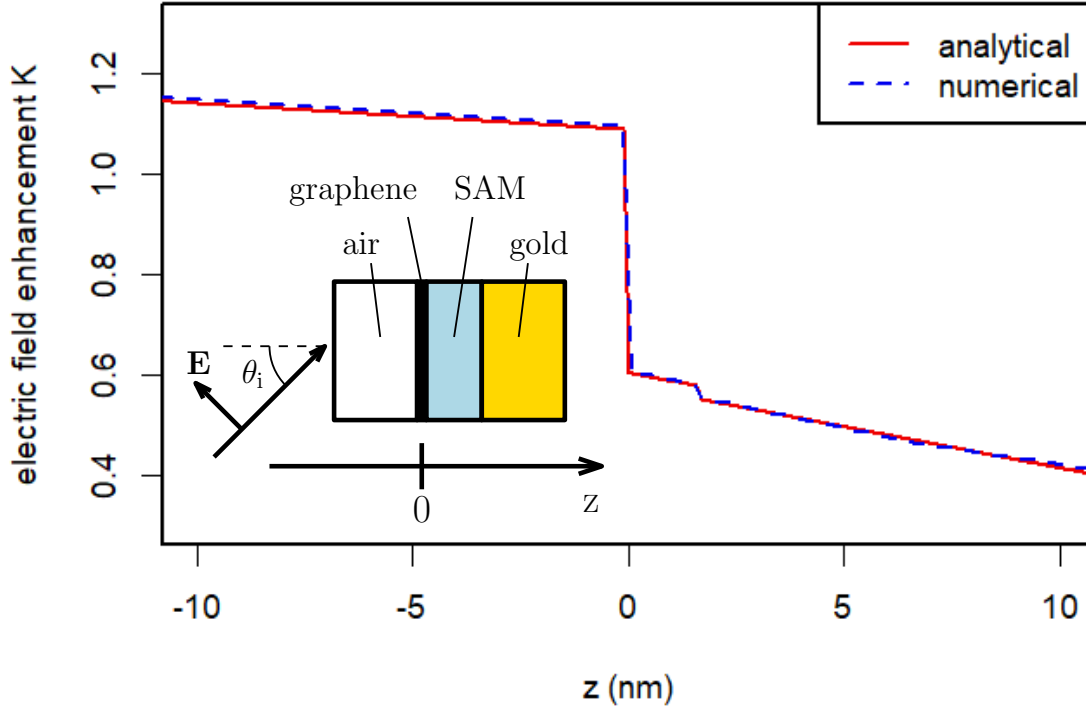


Figure 3.2: Comparison of the analytical and numerical results for the distribution of the electric field along the normal axis of the multilayer system described in chapter 2. The excitation is a plane wave of wavelength 638 nm propagating in air (negative z in the figure) towards the substrate (positive z) at an angle $\theta_i = 30^\circ$ with respect to the surface normal. At $z = 0$ nm a graphene layer is found (described by σ_{gph} from Eq. 2.1), the molecular layer ($n = 2.25$) is situated between $z = 0$ and $z = 1.6$ nm, and the interface between the molecular layer and a semi-infinite gold layer (n from [30]) is at $z = 1.6$ nm.

The comparison between the analytical and numerical solution is shown in Fig. 3.2. The system consist of, from left to right, air, a graphene layer, a 1.6 nm thick molecular layer and a thick gold layer. The system is excited by a plane wave of $\lambda = 638$ nm incoming from air and characterized by an angle of incidence $\theta_i = 30^\circ$ with respect to the surface normal. The distribution of the electric field enhancement $K = |\mathbf{E}| / |\mathbf{E}_0|$ is almost identical (the difference is lower than 1 %) for the analytical (red solid line) and numerical (blue dashed line) solution. Similar agreement is obtained when we consider the parallel or perpendicular component of the fields instead of the amplitude.

4. Tip-enhanced spectroscopy calculations

In this chapter we present the results of the calculations of the optical response of the tip-substrate system described in section 2.1, with a particular focus on the effect of including a graphene layer over a molecular monolayer for tip-enhanced Raman spectroscopy (TERS) and surface-enhanced infrared absorption (SEIRA) experiments. TERS is first discussed in section 4.1, while SEIRA is considered in section 4.2.

4.1. Tip enhanced Raman spectroscopy calculations

In order to characterize and assess the influence of graphene in the electromagnetic enhancement in TERS we need to carry out the calculations for the model geometry both with and without graphene (as described in section 2.1). We first discuss in detail the case without graphene, to later analyze the response of the same system when the graphene layer is included.

4.1.1. Effect of the tip enhancement

To study the response of our system we first obtain the electric field enhancement $K = |\mathbf{E}|/|\mathbf{E}_0|$, corresponding to the amplitude of the total induced field normalized by the

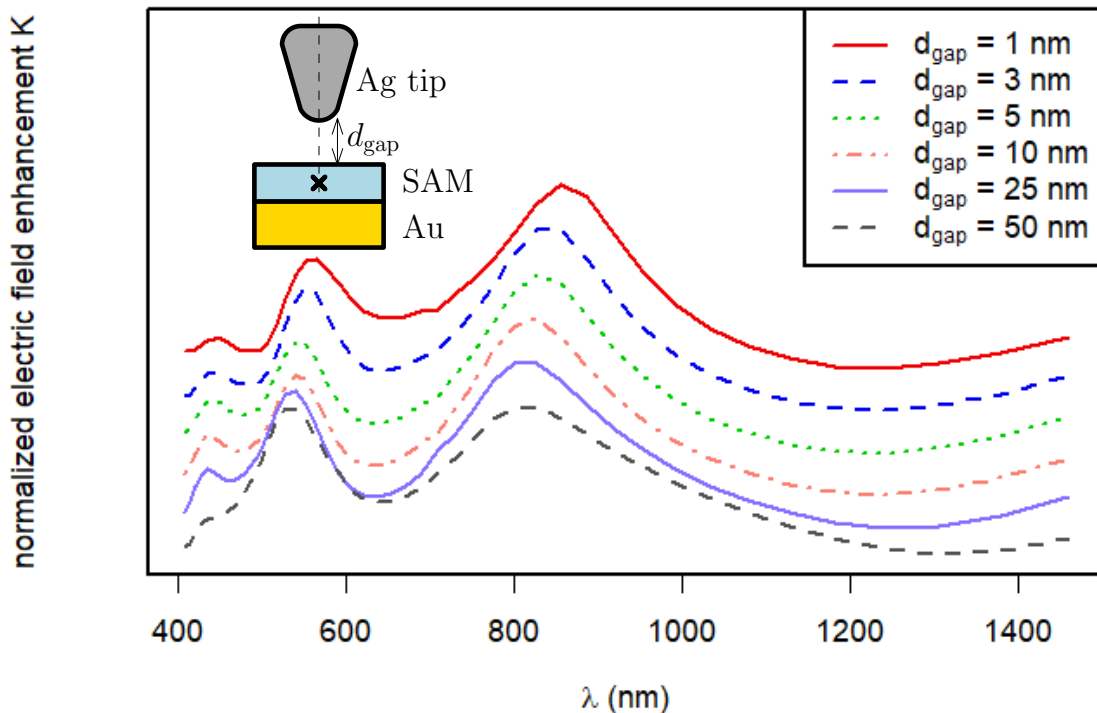


Figure 4.1: Field enhancement spectra for the system without graphene sketched in the inset. We show the values of K in the middle of the layer (marked with a cross), normalized to the maximum of each spectrum and shifted vertically for clarity. We plot the spectra for different gap sizes d_{gap} from 50 nm (bottom spectrum) to 1 nm (top spectrum).

4.1. TIP ENHANCED RAMAN SPECTROSCOPY CALCULATIONS

amplitude of the excitation field (plane wave). As we discussed previously, the TERS enhancement at a given position is approximately proportional to the fourth power of the enhancement K .

We plot in Fig. 4.1 the normalized spectra of K in the middle of the molecular layer immediately below the tip apex (we define this point as $x = 0$ nm, with x being the axis parallel to the surface and p-polarized light propagating in xz -plane), for the distance between the tip and the molecular layer d_{gap} going from 1 nm to 50 nm. Each spectrum in Fig. 4.1 is normalized by dividing by its maximum and then vertically shifted for clarity. For $d_{\text{gap}} = 50$ nm (violet dashed line) the tip-substrate interaction is weak and the spectral position of the localized plasmonic modes of the tip is little affected by the substrate. The peak with the lowest energy (corresponding to a simple dipolar mode of the finite tip) lies in the infrared region at a wavelength around $\lambda = 2000$ nm and we describe it in the section 4.2 when discussing SEIRA. Other peaks can be seen in the spectra at wavelengths around 810 nm, 530 nm and 430 nm, with full-width half-maximum (FWHM) around 160 nm, 80 nm and 40 nm, respectively. The enhancement is highest at wavelengths 530 nm and 810 nm (both maxima corresponding to a similar enhancement). As the tip is approached towards the molecules, the electromagnetic interaction between the tip and the gold substrate increases and all the peaks experience a redshift (lowering of their energy) in a similar way as the bonding mode in the sphere dimer discussed in section 1.1.3. The redshift is approximately 50 nm, 30 nm and 20 nm for the peaks at $\lambda \approx 810$ nm, 530 nm and 430 nm. The redshifts are smaller than the FWHM, so that if the laser is tuned to one of the peaks for $d_{\text{gap}} = 1$ nm, this system is still excited efficiently even

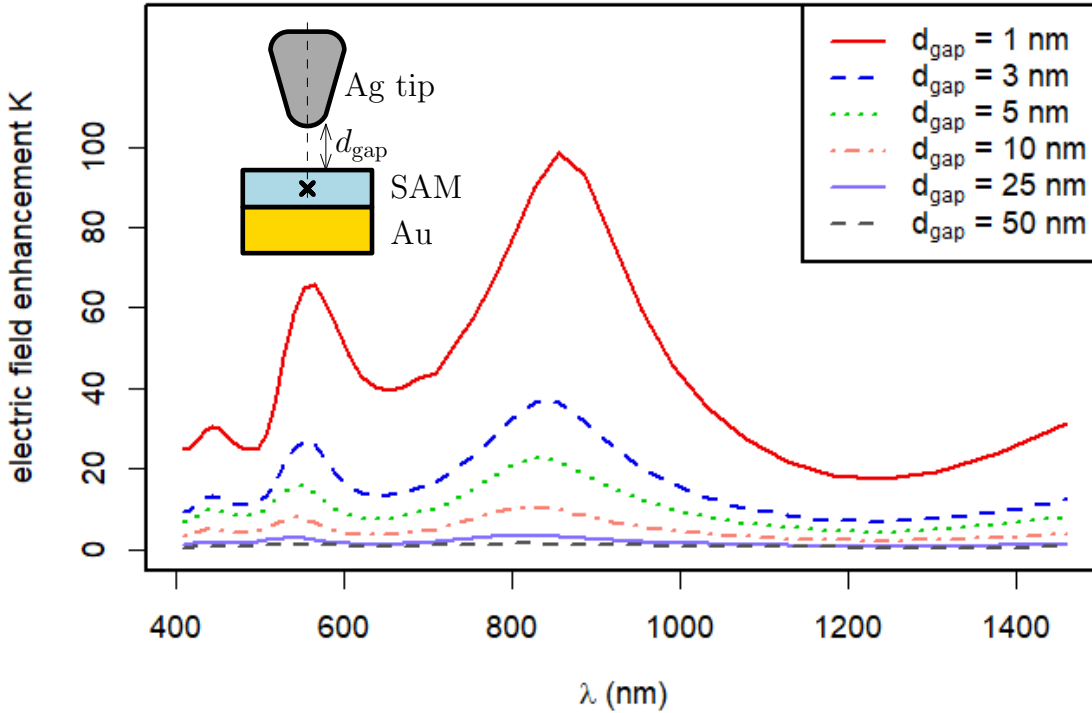


Figure 4.2: Field enhancement spectra for the system without graphene sketched in the inset. We plot the spectral dependence of the electric field enhancement K on the gap size d_{gap} . The fields are calculated at the point in the middle of the layer of molecules just beneath the tip apex (marked with a cross).

4. TIP-ENHANCED SPECTROSCOPY CALCULATIONS

for the largest separation distance. Decreasing d_{gap} also changes the ratio between the maxima of the different resonances, so that the peak originally around 810 nm becomes more prominent for narrow gaps.

The normalized fields in Fig. 4.1 are useful to understand the spectral shift of the modes, but for TERS it is necessary to analyze the magnitude of the enhancement. Thus, in Fig. 4.2, we plot the same field enhancement spectra but without normalization. For large distances the enhancement is small. Specifically for a 50 nm gap the enhancement is about 1.5 for the peaks at 530 nm and 810 nm and around 1 at non-resonant wavelengths. For reference, the enhancement inside the layer in the absence of the tip for $\lambda = 638$ nm can be seen in Fig. 3.2 and is $K = 0.6$. For narrower gaps the enhancement increases very fast as the gap becomes smaller, reaching peak values around 66 and 99 at $\lambda = 560$ nm and 860 nm for 1-nm gap. For non-resonant wavelengths, a clear enhancement is also observed for such short distances, of the order of 10 for $d_{\text{gap}} = 1$ nm. The total enhancement is thus a combination of the excitation of plasmonic modes and of the lightning-rod effect, i.e. the accumulation of charges at the apex of a sharp tip due to the strong potential gradients induced by the geometry that results in strong fields even for wavelengths between the resonance maxima. For experimental tips, that are much larger than those simulated here

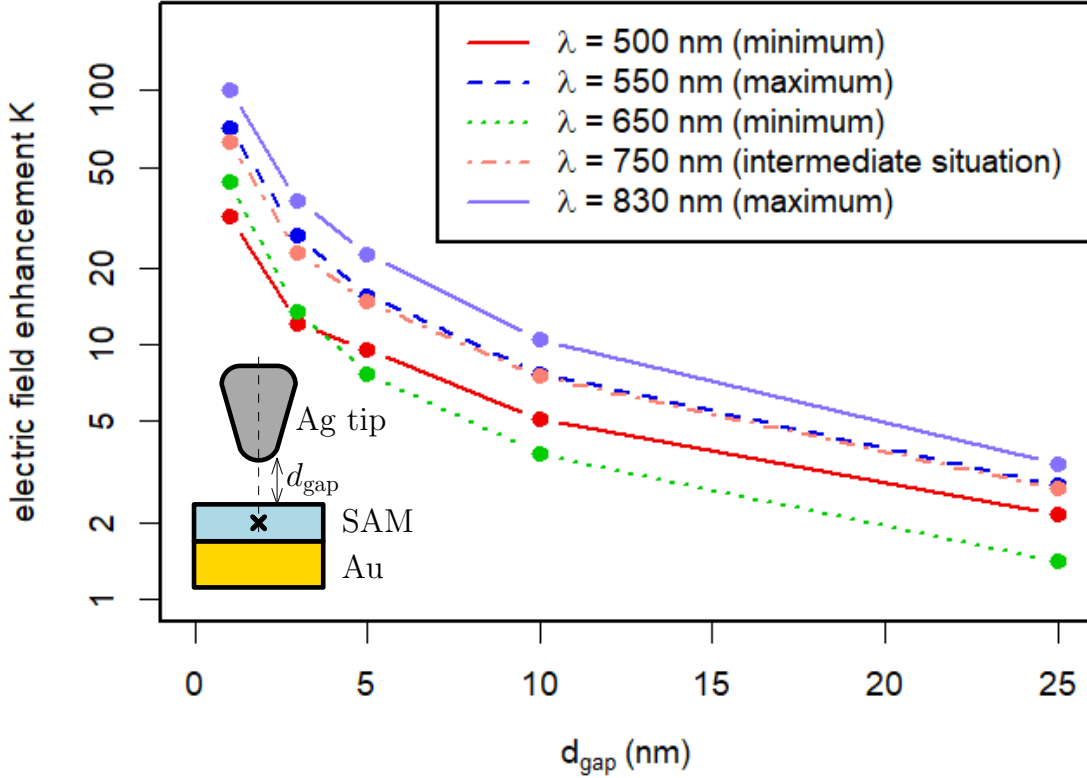


Figure 4.3: Field enhancement dependence for the system without graphene sketched in the inset. We show the dependence of the field enhancement K on the gap size d_{gap} for five selected wavelengths corresponding to two maxima (550 nm and 830 nm), two minima (500 nm and 650 nm) and an arbitrarily chosen wavelength (750 nm). The results are calculated at the point in the middle of the layer of molecules just beneath the tip apex (marked with a cross).

4.1. TIP ENHANCED RAMAN SPECTROSCOPY CALCULATIONS

and that can present rough surfaces, the relative contribution of the plasmonic modes or the lightning-rod effect depends on the exact geometrical details of the tip.

To better discern the dependence of the enhancement with tip-sample separation distance, in Fig. 4.3 we plot the same data but as a function of increasing gap distance for 5 selected wavelengths, corresponding to the two maxima at around 550 nm and 830 nm, the two minima at around 500 nm and 650 nm and an arbitrarily chosen wavelength 750 nm (as the position of the maxima and minima depends on the gap distance, we have chosen an average wavelength for each). The distance dependence of the field enhancement K is very similar for all the wavelengths. The very fast decrease of the signal with distance (notice the logarithmic scale in the y axis) emphasizes that in experiments it is very important to place the tip very close to the sample (a few nanometers) to obtain a strong signal (the enhancement decreases by an order of magnitude when changing the gap size from 1 nm to 10 nm).

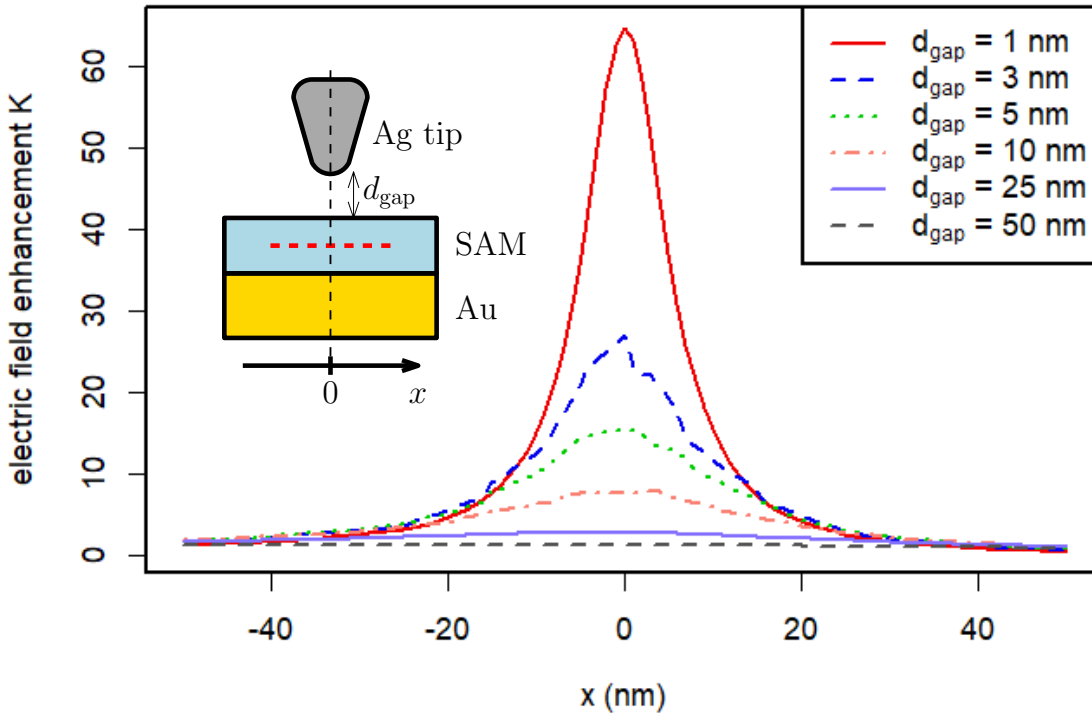


Figure 4.4: Distribution of the electric field for the system without graphene sketched in the inset. We plot the field enhancement K in the middle of the layer of molecules (red dashed line in the inset) for $\lambda = 550$ nm and different distances d_{gap} of the tip from the molecules. The tip apex is located at $x = 0$ nm. Small fluctuations in the spectra are due to numerical noise.

In experiments, the Raman signal originates in the whole layer of molecules, hence it is important to also consider the spatial localization of the field near the tip apex. We plot in Fig. 4.4 the field enhancement as a function of the position along the x axis within 50-nm distance from the position just beneath the tip apex ($x = 0$ nm), again calculated in the middle of the molecular layer. The illumination wavelength $\lambda = 550$ nm corresponds to the resonance in Fig. 4.2 that shifts from $\lambda = 530$ nm at $d_{\text{gap}} = 50$ nm to $\lambda = 560$ nm at $d_{\text{gap}} = 1$ nm. In all the spectra we see a single peak that extends over a region of several tens of nanometers, decreasing very fast as the distance from

4. TIP-ENHANCED SPECTROSCOPY CALCULATIONS

the center is increased. A slight asymmetry due to the tilted illumination (Fig. 2.1a) can be observed. Notably, the localization in the spatial distribution is narrower and more intense for shorter tip-sample separation distances (FWHM of around 12 nm and enhancement of 66 for $d_{\text{gap}} = 1$ nm, compared with FWHM ≈ 25 nm and enhancement of 15 for $d_{\text{gap}} = 5$ nm). Thus, approaching the tip to the molecules leads to much stronger enhancement at the optimal position $x = 0$ nm (Fig. 4.3). On the other hand, larger d_{gap} can result in stronger fields at points further away from the tip (even though the enhancement is lower than 5).

The integrated TERS signal will be affected differently by the two trends with changing d_{gap} shown in Fig. 4.3 and Fig. 4.4. Smaller values of d_{gap} enhance the field much more strongly in a small area under the tip, but at larger distances from $x = 0$ nm, the enhancement is weaker, contributing less to the total TERS signal. We thus integrate the TERS enhancement K^4 (discussed in chapter 2) over the molecular layer (the integral extends over the molecular layer thickness and over a square of 200-nm side, centered below the tip apex). To obtain a dimensionless Raman enhancement $\Gamma_{\text{enh}}^{\text{TERS}}$, this value is further normalized by the volume of the integration region:

$$\Gamma_{\text{enh}}^{\text{TERS}} = \frac{\int K^4 dV}{V}. \quad (4.1)$$

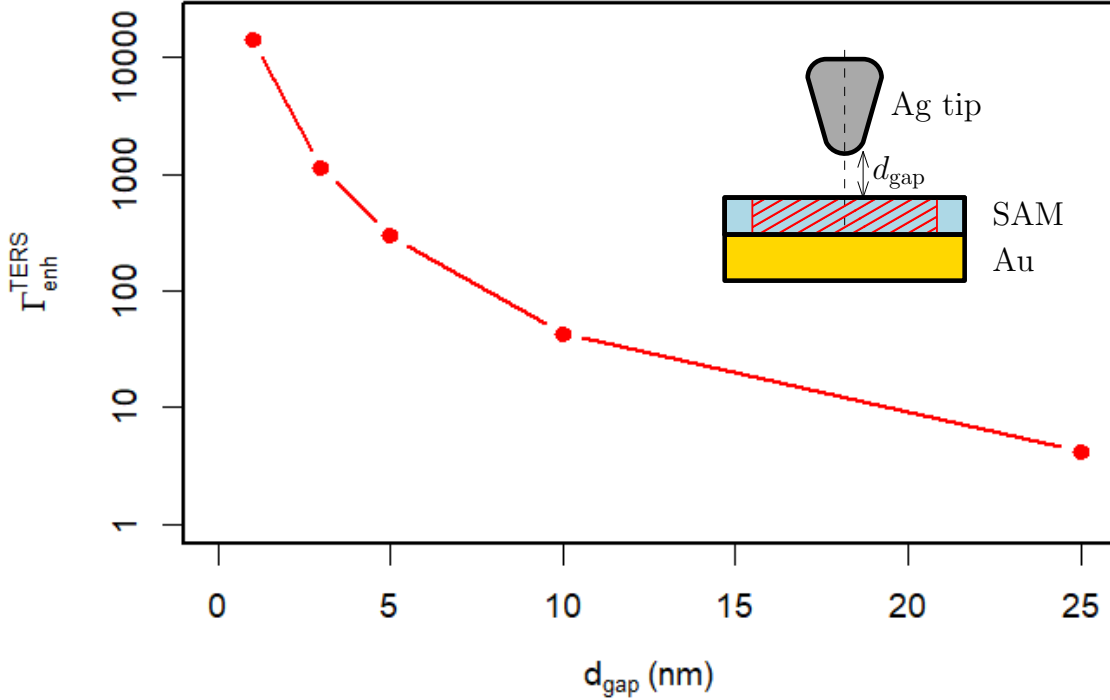


Figure 4.5: Raman spectroscopy signal enhancement (volume-averaged fourth power of the field enhancement) calculated for the system without graphene sketched in the inset, integrated over the molecular layer and normalized by the volume of integration (marked with a hatched area). The integral (Eq. 4.1) is obtained as a function of the separation distance d_{gap} between the tip and the molecular layer for $\lambda = 550$ nm. The integral extends vertically over the full molecular layer and laterally over a box with dimensions $x, y \in (-100, 100)$ nm centered below the tip apex.

4.1. TIP ENHANCED RAMAN SPECTROSCOPY CALCULATIONS

Fig. 4.5 gives the values of the Raman enhancement $\Gamma_{\text{enh}}^{\text{TERS}}$ for $\lambda = 550$ nm (corresponding to a plasmonic resonance). For $d_{\text{gap}} = 1$ nm the enhancement is of the order of 10^4 . The enhancement of the Raman signal decreases very fast, for example, the signal decreases by an order of magnitude as the gap size increases just by 2 nm (from 1 nm to 3 nm) and another order of magnitude as d_{gap} further increases by 4–5 nm. Thus, the signal for a small tip-surface distance is both stronger and more confined than in the case of the tip being further away, thus allowing to obtain a stronger signal from the molecules and better spatial resolution.

4.1.2. Effect of graphene

We consider next the effect of including a layer of graphene on top of the molecules (see section 2.1) in the TERS experiments. Notably, the conductance of graphene, and thus its possible impact on experiments, depends on its Fermi level E_F (Eq. 2.1), which can be tuned on demand (section 1.1.2). We thus consider different values of E_F .

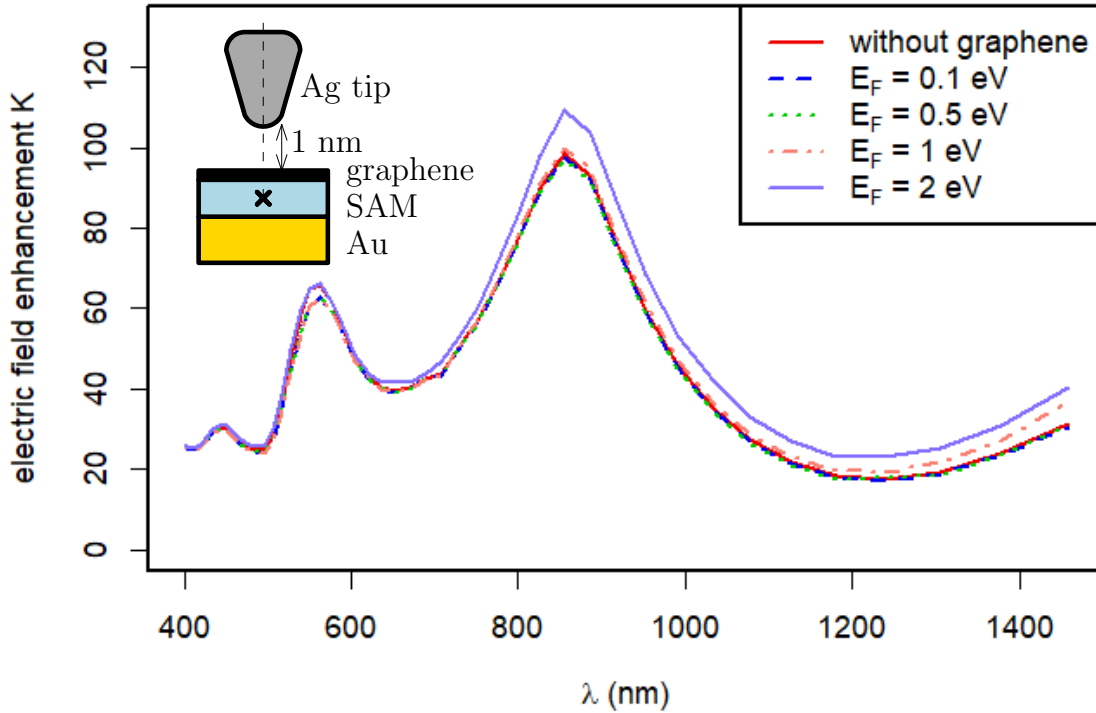


Figure 4.6: Field enhancement spectra for the system sketched in the inset, where a layer of graphene is deposited on top of the molecules. We plot the field enhancement K at the point situated in the middle of the layer just below the tip (marked with a cross). We use $d_{\text{gap}} = 1$ nm distance between the tip and the graphene and change the value of the Fermi level E_F from 0.1 eV to 2 eV. For comparison, we also plot the results in the absence of graphene (red solid line).

To illustrate the effect of the presence of graphene, we obtain the spectra of the electric field enhancement K in the middle of the molecular layer at the point just below the tip, for values of E_F going from 0.1 eV to 2 eV (Fig. 4.6). The tip-separation distance is

4. TIP-ENHANCED SPECTROSCOPY CALCULATIONS

$d_{\text{gap}} = 1$ nm. The solid red line corresponds to the results without graphene (same values as the red line in Fig. 4.2). For Fermi levels of 1 eV and less the introduction of the graphene layer affects the spectra very weakly, with the difference between the spectra with and without graphene being almost unnoticeable. A slightly larger difference is observed for Fermi levels of 1.5 eV and higher, particularly for $\lambda \approx 830$ nm. For this wavelength, the value of K for $E_F = 2$ eV is about 11 % larger than for the case without graphene.

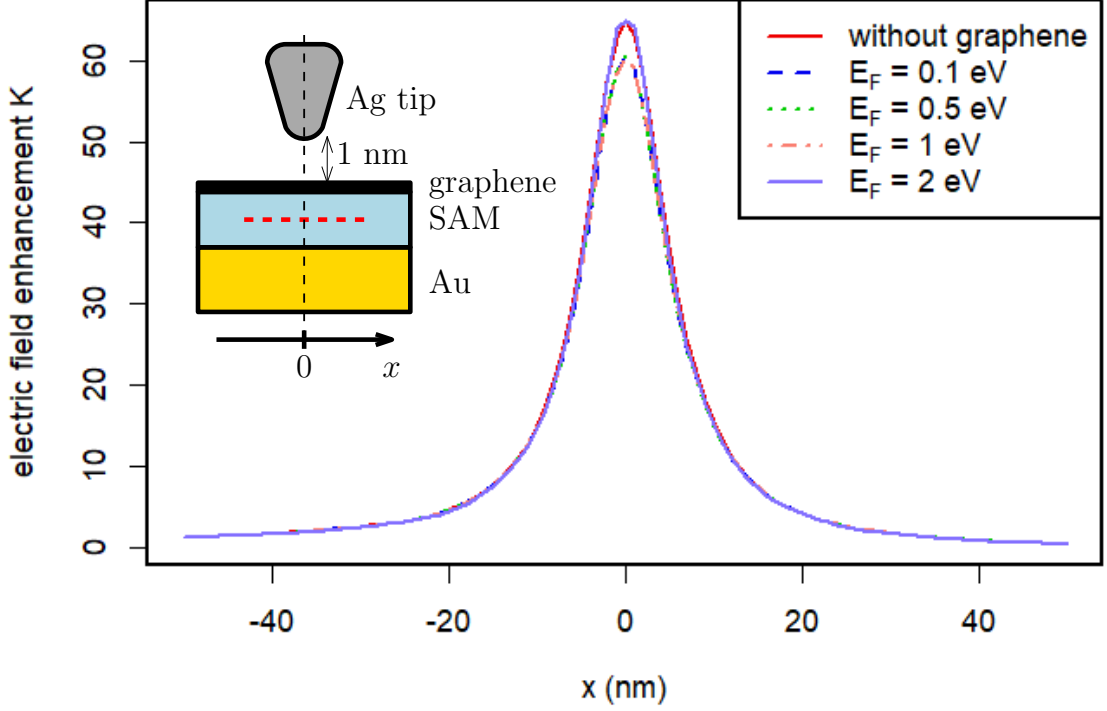


Figure 4.7: Distribution of the electric field for the system sketched in the inset, where a layer of graphene is deposited on top of the molecules. We plot the field enhancement K in the middle of the layer of molecules (red dashed line in the inset) for $\lambda = 550$ nm and tip-separation distance $d_{\text{gap}} = 1$ nm. We consider values of the Fermi level E_F from 0.1 eV to 2 eV and, for comparison, we also plot the results in the absence of graphene (solid red line). The tip apex is located at $x = 0$ nm.

We obtain a similar behaviour when we calculate the electric field enhancement along a line (x axis) in the middle of the molecular layer, as shown in Fig. 4.7. The fields are obtained at one of the maxima of the response, at $\lambda = 550$ nm, and we again compare the results for several values of E_F and without graphene. Similar to the previous result, the difference in the response due to the presence of graphene is quite small; the maximum enhancement reads 66 for case without graphene and with graphene with $E_F = 2$ eV, for other considered values of Fermi energy the field enhancement K is approximately 63.

We thus conclude that introducing the graphene layer induces a very weak change on the electromagnetic TERS enhancement. Furthermore, the larger Fermi levels considered can be difficult to reach in experiments. Graphene does not affect the results of the enhancement likely because in the visible region it usually acts as a simple transparent

4.2. EFFECT OF GRAPHENE IN SEIRA

layer [37], only slightly modifying the reflection and absorption of the multilayer system, with no graphene SPPs being excited [37]. We stress that in this thesis we only consider the electromagnetic enhancement and thus assume that the graphene layer does not modify the chemical structure of the molecules. To fully predict the results that would be obtained in an experiment, other effects need to be considered, such as the chemical mechanism of GERS, or morphological modifications in the molecular layer when the graphene is deposited.

4.2. Effect of graphene in SEIRA

So far we have presented the results of calculations in the visible region of the spectra, which showed that graphene provides a small electromagnetic (plasmonic) effect in TERS. Graphene might have, nevertheless, an influence in the optical response in the infrared region of the spectra, where the energy of the illuminating light $\hbar\omega$ can be sufficiently low to excite SPPs in graphene. Thus, the presence of graphene (and its Fermi energy E_F) might influence the signal in SEIRA. We discussed in section 2.1 how the SEIRA signal is related to the enhancement of the local intensity K^2 . To examine the effect of graphene, however, we first focus simply on the electric field enhancement K .

We show in Fig. 4.8 the field enhancement K spectra for the different values of the Fermi energy of graphene E_F (ranging from 0.1 eV to 2 eV). We plot the spectra from $\lambda = 1240$ nm to $\lambda = 12400$ nm, corresponding to energies 1–0.1 eV (which complements the

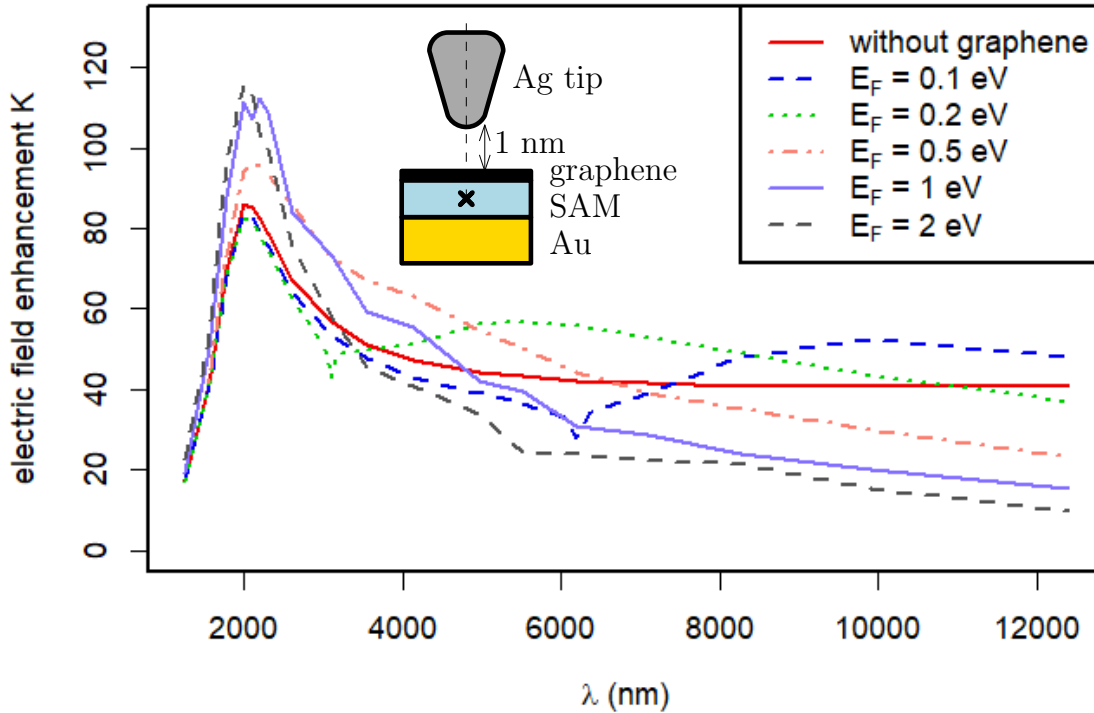


Figure 4.8: Spectra of the field enhancement K for the system sketched in the inset, where a layer of graphene is deposited on top of the molecular layer. The enhancement K in the point situated in the middle of the layer just below the tip (marked with a cross) is plotted for Fermi energies E_F from 0.1 eV to 2 eV and infrared illumination, and compared to the system without graphene (red solid line).

4. TIP-ENHANCED SPECTROSCOPY CALCULATIONS

results for lower wavelengths in Fig. 4.6). We use the same geometry as for TERS, except for the frequency range under investigation (Fig. 2.1b). We also show for comparison the results in the absence of graphene (red solid line). The tip is located at $d_{\text{gap}} = 1$ nm distance from the surface of the molecular layer, and we evaluate again the fields at a position below the tip apex ($x = 0$ nm) in the middle of the molecular layer. All the spectra show a peak at $\lambda \approx 2100$ nm, which corresponds to the dipolar mode of the structure. The value at the maximum is similar for the case without graphene ($K = 86$) and with graphene with low Fermi energy ($K = 83$ for both $E_F = 0.1$ eV and $E_F = 0.2$ eV). For $E_F = 0.5$ eV the enhancement takes a value of 96 and then it finally grows to 112 and 115 for $E_F = 1$ eV and 2 eV, respectively.

At higher wavelengths we also observe the influence of graphene and of its Fermi energy on the enhancement. The field enhancement in the case without graphene (red solid line in Fig. 4.8) becomes approximately constant for $\lambda \gtrsim 6000$ nm, with values $K \approx 41$. However, in the presence of graphene with the Fermi energy of 0.5 eV and higher, the enhancement (that is stronger than in case without graphene at $\lambda = 2100$ nm) generally decreases with increasing wavelength, finally becoming weaker than for the case without graphene; this decrease is more pronounced for higher Fermi energies (minimum

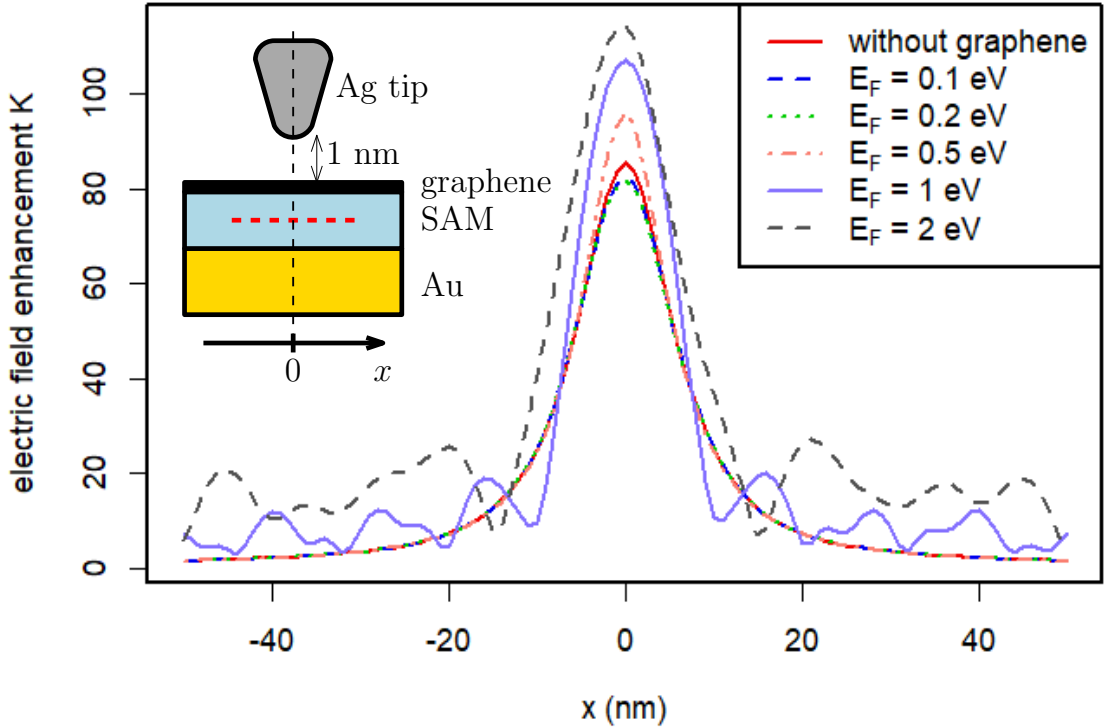


Figure 4.9: Distribution of the electric field for the system sketched in the inset, where a layer of graphene is deposited on top of the molecules. The enhancement is measured in the middle of the layer of molecules (marked with a red dashed line in the inset) for $\lambda = 2100$ nm and $d_{\text{gap}} = 1$ nm. The tip is located at $x = 0$ nm. We plot the enhancement K for different values of the Fermi level E_F from 0.1 eV to 2 eV and also for the case without graphene (solid red line). The oscillations in the spectra for $E_F = 1$ eV and 2 eV are probably related to numerical errors in calculations.

4.2. EFFECT OF GRAPHENE IN SEIRA

value in displayed spectra is $K = 10$ for $E_F = 2$ eV at $\lambda = 12000$ nm). Nonetheless, the case is different for Fermi energies $E_F = 0.1$ eV and 0.2 eV: at lower wavelengths the spectra follow the red line corresponding to the system without graphene until they reach illumination energy $\hbar\omega = 2E_F$. At these energies an abrupt change of the graphene conductivity occurs (Eq. 2.1) and a dip appears in the spectra. After that, for longer wavelengths in a specific region the enhancement becomes stronger in comparison to the case without graphene ($K = 53$ for $E_F = 0.1$ eV around $\lambda = 10000$ nm and $K = 57$ for $E_F = 0.2$ eV around $\lambda = 5500$ nm). For higher wavelengths the enhancement starts to decrease similarly as in the spectra for higher Fermi energies. We believe that this behaviour is in fact the same for all cases, we just don't notice the dip in the spectra at lower wavelengths (explaining stronger enhancement at $\lambda = 830$ nm for $E_F = 2$ eV and at $\lambda = 2100$ nm for $E_F = 0.5 - 2$ eV). The increase might be caused by the absence of interband transitions in graphene for $\hbar\omega < 2E_F$, resulting in smaller losses, however, other losses eventually prevail for longer wavelengths.

To better understand these results, we plot in Fig. 4.9 the spatial distribution of the electric field enhancement K in the middle of the molecular layer under the tip. We plot the results along the x axis for $d_{\text{gap}} = 1$ nm and $\lambda = 2100$ nm (maximum in the spectra). The response for Fermi energies $E_F = 0.1 - 2$ eV are again compared with the results when no graphene is present. In cases without graphene and with graphene with Fermi energies $E_F = 0.1 - 0.5$ eV the distribution of the electric field enhancement beneath the tip is similar (with FWHM of about 12 nm). However, for $E_F = 1$ eV

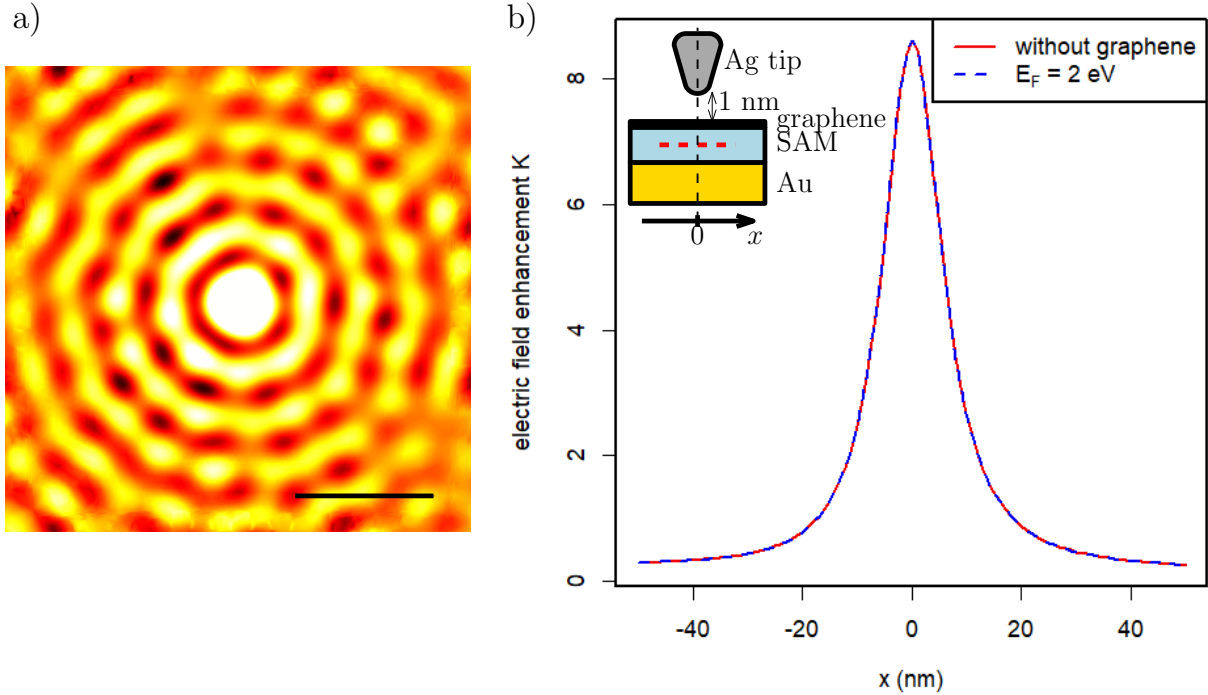


Figure 4.10: Results discussing further the electric field spatial distribution. (a) E_z component of the electric field (perpendicular to the sample) in xy -plane in the middle of the molecular layer shows a circular pattern (E_z selected for the best visibility). The black bar has a length of 50 nm. (b) Spatial distribution of the electric field enhancement in 2D calculations along a line in the middle of the layer of molecules (red dashed line in the inset) for $\lambda = 2100$ nm and $d_{\text{gap}} = 1$ nm with the tip located at $x = 0$ nm.

4. TIP-ENHANCED SPECTROSCOPY CALCULATIONS

(FWHM ≈ 12 nm) and $E_F = 2$ eV (FWHM ≈ 15 nm) we observe an increased field enhancement further away from the tip, which oscillates with an increasing distance. At first glance one might say that these results would indicate an excitation of SPPs in graphene, yet we rather disagree with this interpretation for number of reasons. The distribution of the electric field enhancement of a propagating SPP would not oscillate with an increasing distance from the tip, but rather only decrease (K is a ratio of electric field amplitudes, which don't oscillate). These oscillations would arise if multiple waves were present, such as in case of a standing wave, which would be caused by a reflection of the SPP from a boundary or a region with a very different mesh element size in the simulation domain. In our calculations we truly observe a change in the field enhancement distribution oscillations when parameters associated with the size of the simulation domain are changed. Nonetheless, as we use only rectangular boundaries and regions with different mesh settings, the SPP standing wave pattern would show a fourfold symmetry, but the pattern observed in our calculations (Fig. 4.10a) is composed of concentric circles. The explanation based on beats of multiple SPPs or on a periodical transfer of energy along the z -direction is also disproved by the aforementioned changes in distribution for different simulation domain sizes. Moreover, we also carrier out a similar simulation in 2D, where the cross-section through the geometry was the same as in 3D (Fig. 2.1), but in the third dimension the model differs (the tip is an infinite prism rather than a cone). The distribution of the electric field enhancement along the x axis for $d_{\text{gap}} = 1$ nm and $\lambda = 2100$ nm (Fig. 4.10b) for a case without graphene and with graphene with $E_F = 2$ eV looks almost identical, i.e. we observe no increased and oscillating values further away from the tip. All these results suggest that the oscillations in the distribution for $E_F = 1$ eV and 2 eV in 3D simulations are caused by a numerical error, which we are not able to get rid of with the available computational resources.

In conclusion, the presence of graphene has an effect on the enhancement of the electric field directly under the tip (as seen in the spectra), increasing the enhancement in a spectral window of illumination energies near the condition $\hbar\omega < 2E_F$ (below the absorption edge of graphene) and then decreasing it for larger wavelengths. The spatial distribution of the electric field enhancement is similar for Fermi energies $E_F = 0.1-0.5$ eV as for the case without graphene, which in turn affects the enhancement of the SEIRA signal simply as K^2 (i.e. the square of values in spectra in Fig. 4.8). For Fermi energies $E_F = 1$ eV and 2 eV the spatial distribution was distorted due to numerical errors.

5. Scanning near-field optical microscope calculations

We discuss in this chapter results of our calculations of the scanning near-field optical microscope model described in section 2.2. We focus on the investigation of the sensitivity of a SNOM probe to different components of the near-field (that takes the form of a surface plasmon polariton standing wave), namely the in-plane component (parallel to the sample surface and perpendicular to the tip axis) and the out-of-plane component (perpendicular to the surface and parallel to the tip axis).

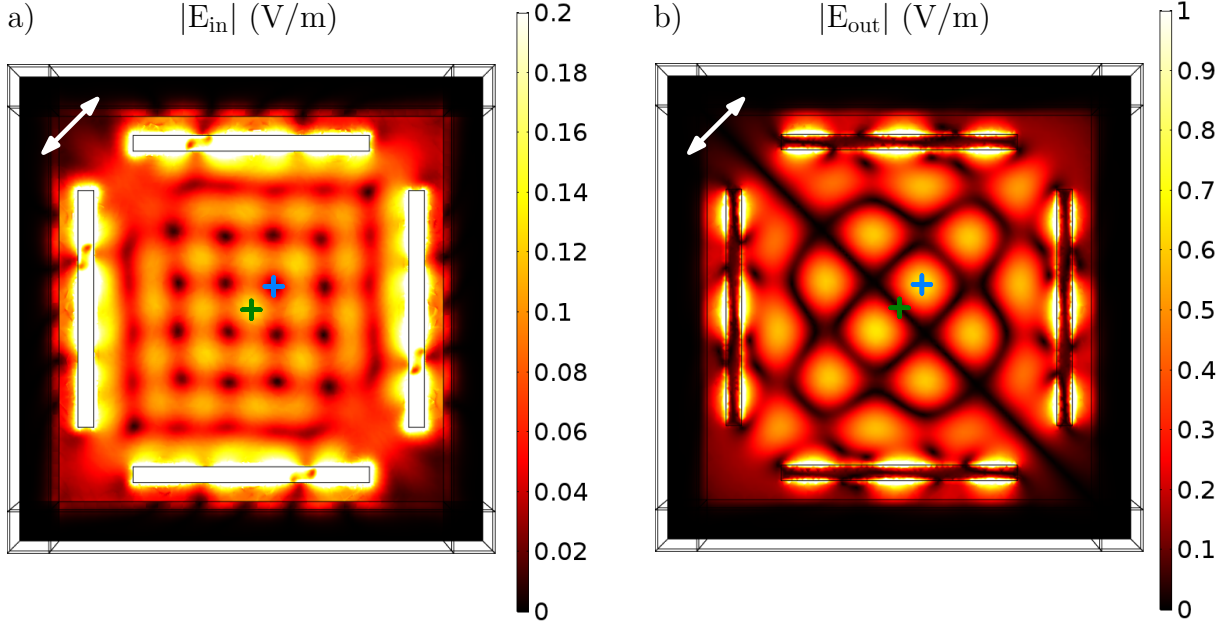


Figure 5.1: Surface plasmon polariton standing wave pattern excited on the gold-air interface without the presence of the tip. (a) Distribution of the in-plane component of electric field with a maximum considered in the following denoted by a green cross at coordinates $[0, 0]$ nm. (b) Distribution of the out-of-plane component of electric field with a maximum considered in the following denoted by a blue cross at coordinates $[140, 140]$ nm. Note the different scales in each image. The values are taken in the distance of 0.1 nm from the gold surface, the distance of the opposite slits is $2 \mu\text{m}$ and the amplitude of the illuminating light with $\lambda = 650 \text{ nm}$ polarized along the diagonal (white double arrow) is $|E_0| = 1 \text{ V/m}$.

As described before, the sample in our model consists of a glass substrate covered with a gold layer with four slits (with dimensions $0.1 \mu\text{m} \times 1.5 \mu\text{m}$) arranged in a square with the side of $2 \mu\text{m}$ (Fig. 2.2b). When the sample is illuminated from the bottom (from the side of the glass substrate, perpendicularly to the sample) the four slits represent sources of surface plasmon polaritons (SPPs) on the top gold surface (the interface between gold and air). In order to excite all the SPPs with the same intensity, the incident light is polarized along the diagonal of the square. Since the slits are arranged into a square, the plasmons inside of the square structure form standing waves, as depicted in Fig. 5.1. In this arrangement of two perpendicular standing waves (originating in the two pairs of slits opposite to each other) regions with maxima of either in-plane or out-of-plane

5. SCANNING NEAR-FIELD OPTICAL MICROSCOPE CALCULATIONS

components emerge due to interference of the two standing waves. The maxima of the in-plane component are always located in the minima of the out-of-plane component and similarly the maxima of the out-of-plane component lie in the minima of the in-plane component, i.e. the component maxima are spatially separated. The out-of-plane component maxima have an amplitude comparable to the amplitude of incident light and the amplitude of the in-plane maxima is about 5 times smaller for the considered setup.

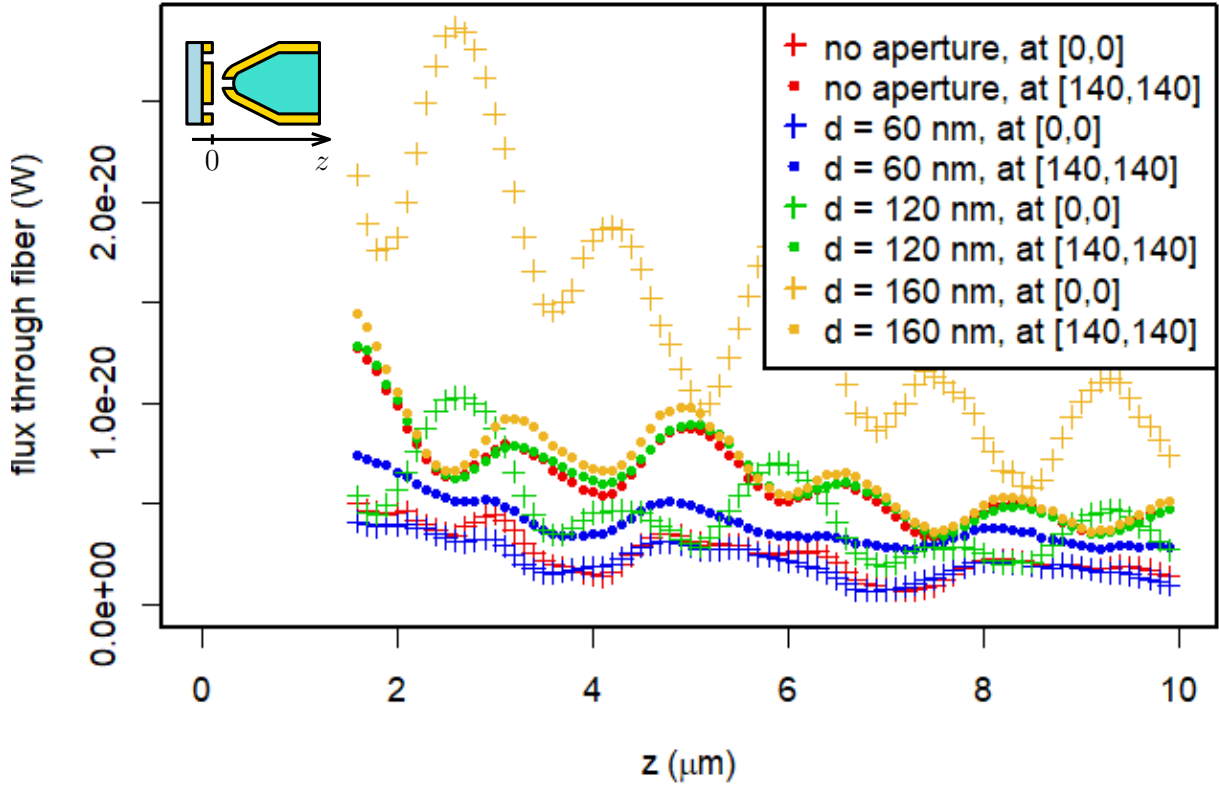


Figure 5.2: Dependence of a total energy flux through the fiber core on the position z along the axis of the fiber (0 corresponds to the sample surface) at which the flux is calculated over the fiber core cross-section. The flux is shown only in the part of the fiber with a constant diameter (cylindrical part). The tip (variants with three different aperture diameters and without an aperture) is positioned either above the in-plane component maximum (crosses, at coordinates $[0,0]$ nm) or the out-of-plane component maximum (dots, at coordinates $[140,140]$ nm) in a 1-nm distance from the sample surface.

In the further analysis of the results of a SNOM probe sensitivity we consider two positions of the tip: the tip is either placed above the in-plane maximum at coordinates $[0,0]$ nm (denoted by a green cross in Fig. 5.1) or above the out-of-plane maximum at $[140,140]$ nm (blue cross in Fig. 5.1). As mentioned in section 2.2, we approximate the measured signal of SNOM as a total energy flux Φ_e through the glass fiber core of the probe, i.e. an integrated Poynting vector over the cross-section of the core (Eq. 2.2). In Fig. 5.2 we show the dependence of the energy flux through the core on the position z along the axis of the core for four different tips (three tips with a different aperture diameter and one apertureless tip) and for positions above in-plane (crosses, marked as $[0,0]$) and out-of-plane maxima (dots, marked as $[140,140]$) with the tip being placed in a distance of 1 nm from the sample. Only about 1 % of the incident power of light

passes through the gold layer and another 2 or 3 orders of magnitude are lost in the coupling into the fiber core. The flux (plotted only for z corresponding to the part of the fiber with a constant diameter, i.e. the cylindrical part) is expected to decrease due to the losses in the coating as the signal propagates through the fiber; however, we observe an oscillating dependence. Upon closer inspection we can see that these oscillations are periodic with a period of approximately $3.3 \mu\text{m}$. We note that we inspect only the flux through the core of the tip, so this behaviour can be caused by an additional energy flux through the 130 nm thick gold coating. In Fig. 5.2 we can see that in the case of a tip with a big aperture diameter of 160 nm the signal above the in-plane maximum is always greater than above the out-of-plane maximum, for an aperture diameter of 120 nm the two dependences cross each other for several values of z and for a small aperture diameter of 60 nm and for an apertureless tip the signal is stronger for the position above the out-of-plane maximum. The dependence of flux over the out-of-plane maximum is similar for three of four presented cases, but for the tip with a small aperture (60-nm diameter) this dependence differs. In explanation of this we have to mention that when we carried out calculations with different dimensions of the simulation domain (in particular, with different lateral size), we obtained different values for all the cases. However, the ratio between signal measured at different positions above the sample stays quite similar. Therefore at least qualitative results can be acquired. The values of flux do

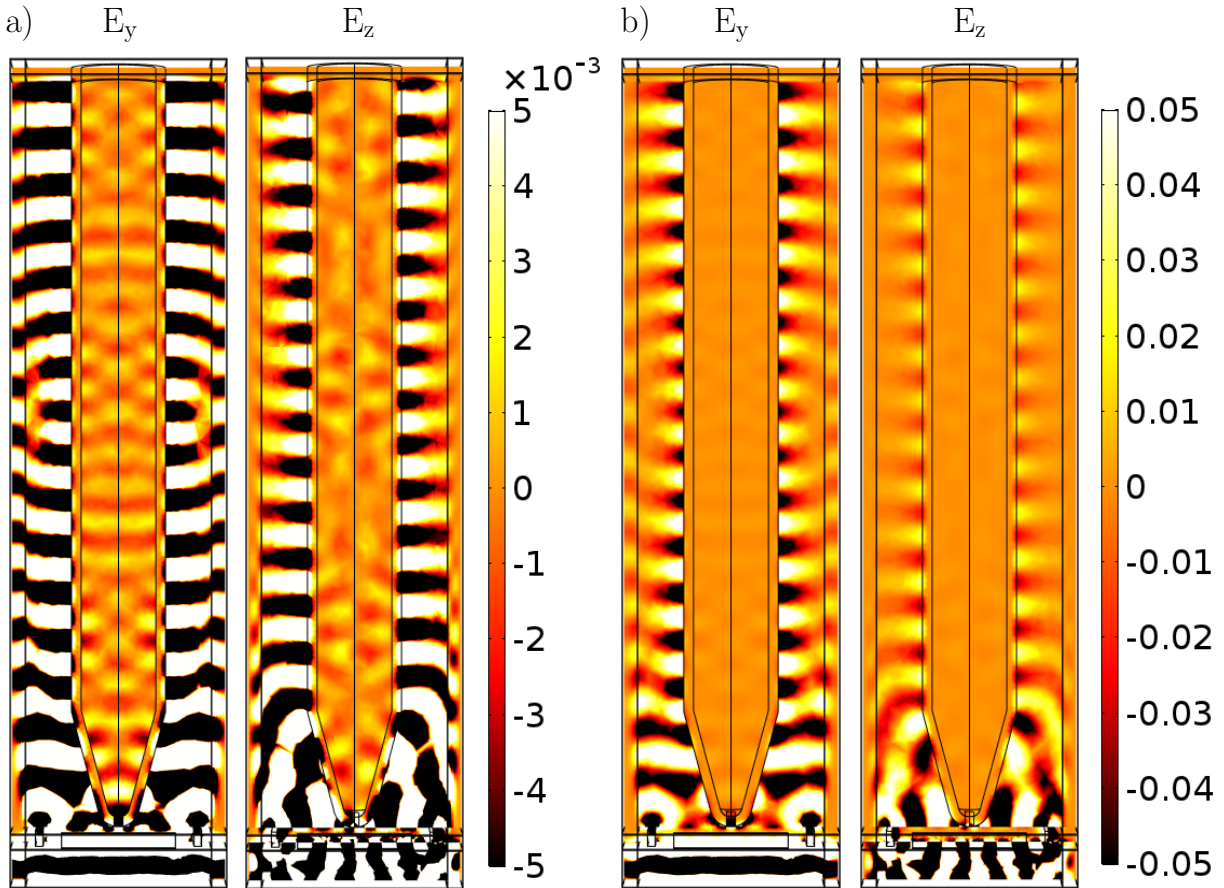


Figure 5.3: Spatial distribution of electric field components E_y and E_z in the yz -plane. The cross-sections go through the axis of the fiber which is positioned above the center of the slit square pattern, i.e. above the in-plane component maximum. The scales are selected to visualize either the field inside (a) or outside (b) the fiber.

5. SCANNING NEAR-FIELD OPTICAL MICROSCOPE CALCULATIONS

not vary in a simple way (i.e. a wider simulation domain does not imply higher or lower values) which leads to an impossibility to obtain quantitative results, since we cannot get converged calculations with the available computational power. Hence the shown values of the flux are only qualitative and the results for the aperture with 60-nm diameter can differ from the others due to numerical inaccuracies.

To get a further insight to the electric field in the fiber and to identify the reason why the flux inside the core oscillates we show in Fig. 5.3 the spatial distribution of electric field components E_y and E_z in the yz -plane cross-section through the axis of the fiber for the case where the tip is positioned above the in-plane component maximum. In Fig. 5.3a the scaling of the field is selected to show the field inside the core. We can see periodic pattern with the same periodicity of around $3.3 \mu\text{m}$ as in the flux oscillations. The field is composed of one or more propagating modes in the fiber and perhaps also of an SPP on the glass-gold interface. Nevertheless, the combination of multiple modes cannot explain the oscillations of the flux. In Fig. 5.3b we depict the field outside of the fiber (with different scaling). From the phase difference of E_y and E_z we can deduce that an SPP is propagating along the outer surface of the gold coating, and in E_y we can see that there are present both the far-field radiation and the SPP (with slightly different wavelength). In a separate simulation of a different model (not shown here) we have confirmed that no power passes through the coating in the perfectly matched layer (PML) at the top end of the fiber. During this calculation we have also found out that the plasmons on the outer coating surface can penetrate through the coating and excite a propagating wave inside the glass core. Naturally, this mechanism is expected to be effective also the other way

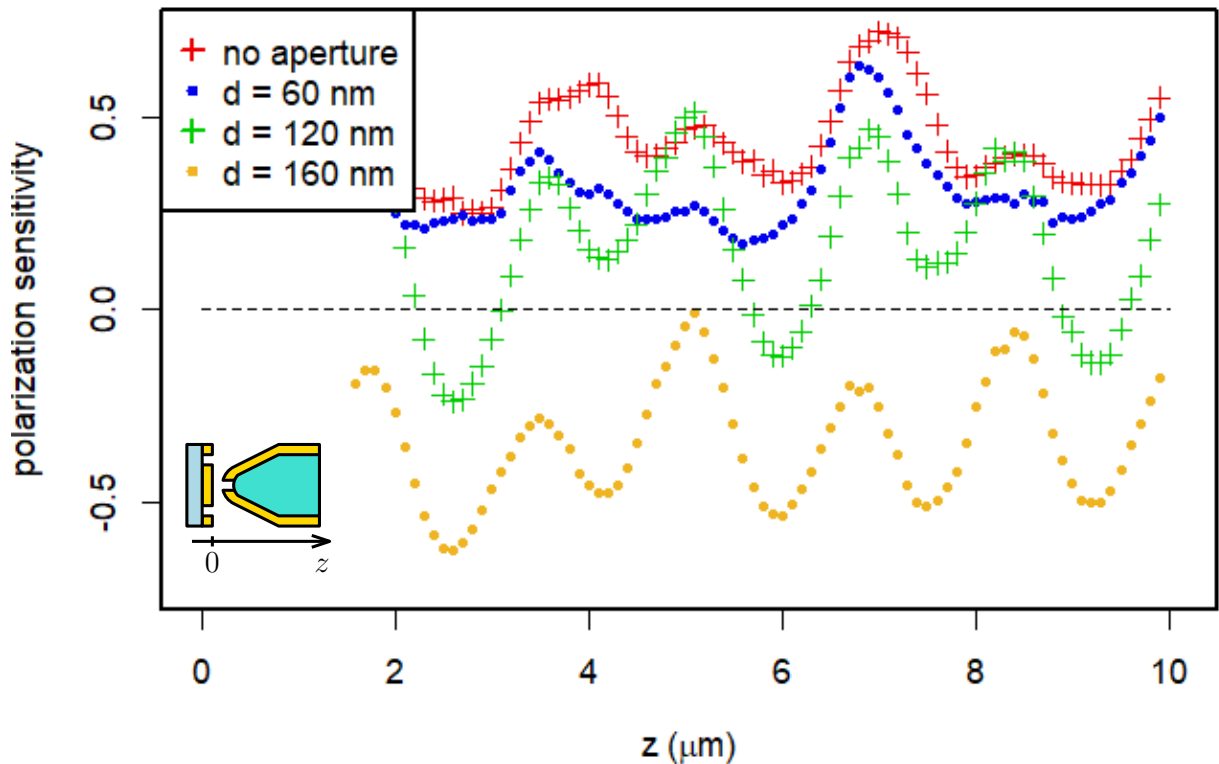


Figure 5.4: Polarization sensitivity of tips with different aperture diameters and of an apertureless tip. The tips are positioned in a distance that corresponds to a 1-nm gap between the tip and the sample for the case without an aperture.

round. We thus believe that the oscillations in the flux are caused by a periodic energy transfer between the propagating modes inside the glass core and the SPP on the outer surface of the gold coating.

As already mentioned, the ratio between values for cases with tip above the in-plane and out-of-plane component maxima stays the same regardless of the width of the simulation domain, i.e. the values are multiplied by the same constant, allowing us to extract qualitative information. Moreover, we are mainly interested in determining which component couples into the fiber more efficiently, that is, whether we detect the in-plane or out-of-plane component (polarization) in experiments. To this end we define polarization sensitivity

$$\nu = \frac{\Phi_{e,\text{out-of-plane}} - \Phi_{e,\text{in-plane}}}{\Phi_{e,\text{out-of-plane}} + \Phi_{e,\text{in-plane}}}, \quad (5.1)$$

where $\Phi_{e,\text{out-of-plane}}$ is the flux calculated over the out-of-plane component maximum and $\Phi_{e,\text{in-plane}}$ is the flux calculated over the in-plane component maximum. The polarization sensitivity ranges from -1 to 1 , where -1 signifies that only the in-plane component is detected (out-of plane component being zero), 1 has the opposite meaning and value of 0 means that both components couple to the tip with equal efficiency. In Fig. 5.4 we

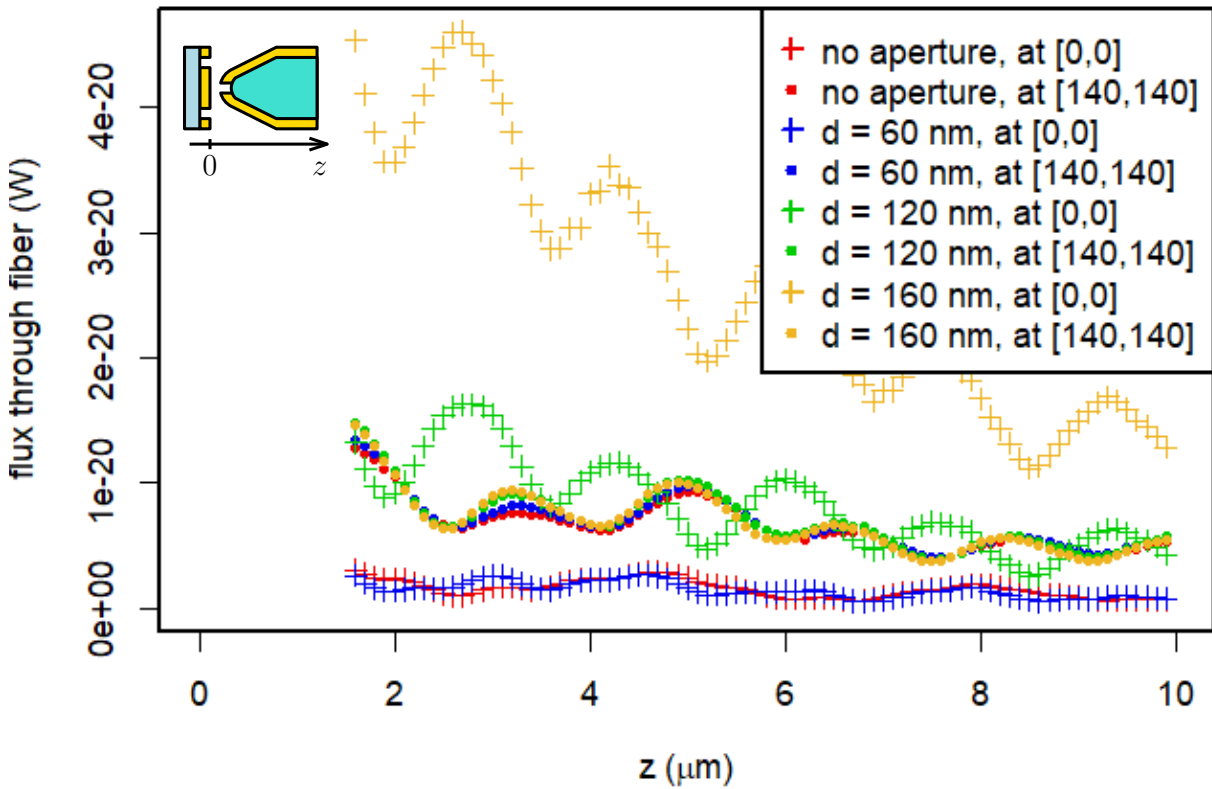


Figure 5.5: Total energy flux through the fiber dependent on the position z along the axis of the core for tips placed in a distance corresponding to a 10-nm gap between an apertureless tip and the sample. Values for four different tips (one apertureless and three with different aperture diameters) positioned above the in-plane component maximum (crosses, at coordinates $[0, 0]$ nm) and the out-of-plane component maximum (dots, at coordinates $[140, 140]$ nm) are shown.

5. SCANNING NEAR-FIELD OPTICAL MICROSCOPE CALCULATIONS

show the polarization sensitivity obtained for the values of the flux from Fig. 5.2. We can see that tips either with small aperture (60 nm in diameter) or without an aperture are more sensitive to the out-of-plane component, a tip with large aperture (160 nm in diameter) shows the signal corresponding more to the in-plane component and the signal obtained with a tip with an aperture diameter of 120 nm exhibits the polarization sensitivity fluctuating around zero.

We also discuss the effect of the distance between the tip and the sample. In Fig. 5.5 we show the energy flux in the fiber core for the same tips as before (an apertureless tip and tips with aperture diameters of 60 nm, 120 nm and 160 nm) positioned in a distance corresponding to a 10-nm gap between the tip and the sample. The dependences look similar to the results for 1-nm gap (Fig. 5.2), except the dependence for the tip with a 60-nm aperture positioned above the out-of-plane component maximum now has the same magnitude as for other tips, and more importantly the values for the tip with the large aperture (with the diameter of 160 nm) placed above the in-plane component maximum are larger. In Fig. 5.6 we plot also the polarization sensitivity calculated from these values, which exhibits again a similar behaviour. However, the overall polarization sensitivity is larger, and thus the tips are even more sensitive to only one component.

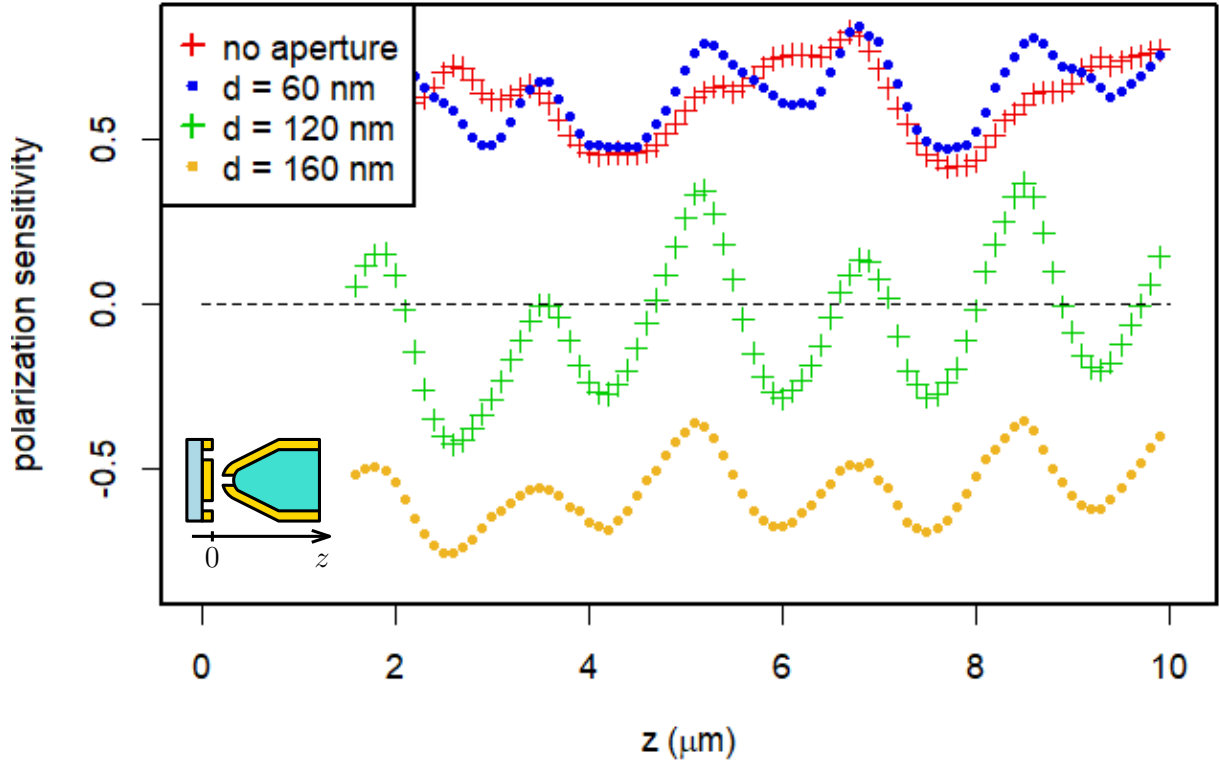


Figure 5.6: Polarization sensitivity of the tips placed in a distance corresponding to a 10-nm gap between an apertureless tip and the sample. Cases with an apertureless tip and three tips with a different aperture diameter are presented.

Finally, the tip properties largely depend on the material of coating. Therefore, in Fig. 5.7 we present the results of the calculated flux for an aluminium coated tip. The coating thickness of 130 nm as well as all the other parameters is kept the same and we place the tip in a 1-nm distance from the sample surface. We compare tips with aperture diameters 60 nm and 120 nm. In both cases the flux above the in-plane component

maximum is much larger (around 10 times larger for 60-nm aperture and around 100 times for 120-nm aperture). The flux for the tip with a larger aperture above the in-plane maximum does not clearly show fluctuations as observed in the case of gold coating, which suggests that the majority of the flux originates at the aperture (energy passing through the aperture). All three other dependences have values lower by two orders of magnitude and the oscillations begin to appear, meaning that the transfer through the coating has a similar magnitude as transfer through the aperture, which again points to the conclusion that the measured flux inside the fiber comes both from the coupling through the aperture and from the transmission through the coating.

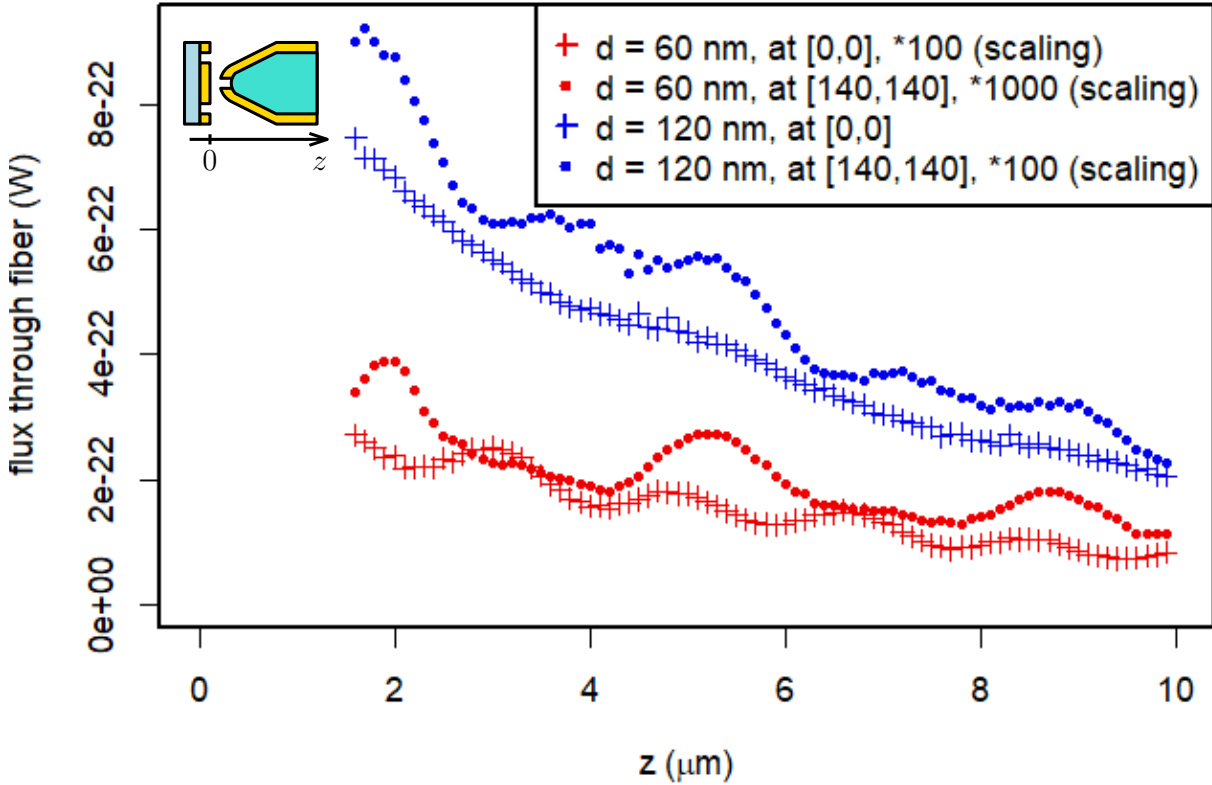


Figure 5.7: Total energy flux through the fiber for an aluminium coated probe. The tip is placed either above the in-plane component maximum (crosses, at coordinates $[0,0]$ nm) or above the out-of-plane component maximum (dots, at coordinates $[140,140]$ nm) in a 1-nm distance from the sample. Note that three of the four dependences were rescaled for better visibility.

In summary, we observe that the SNOM tips with either small aperture (with 60-nm diameter) or without an aperture are more sensitive to the out-of-plane component of the electric field, tips with large aperture (with 160-nm diameter) are more sensitive to the in-plane component, and for the case with the aperture diameter in between (120 nm) the selectivity to one component cannot be determined (the tips are sensitive to both polarizations approximately equally). The signal (energy flux) going through the fiber also depends on the material of the coating, with gold allowing the transmission of the energy through the coating (the contribution of which to the signal is not negligible) leading to fluctuations in the flux, and aluminium not allowing such energy transfer.

6. Conclusion

We perform electromagnetic numerical calculations using the finite element method to analyze two systems. First, the plasmonic response of a silver tip interacting with a molecular layer assembled on a gold substrate is investigated; notably, we study the electromagnetic effect of including a graphene layer on tip-enhanced Raman spectroscopy (TERS) and surface-enhanced infrared absorption spectroscopy (SEIRA) experiments. Second, the selectivity of a scanning near-field optical microscope (SNOM) probe (metal coated glass fiber) to different components of the electromagnetic near-field is inspected, with the near-field having a form of a surface plasmon polariton standing wave with separated areas with either an in-plane or an out-of-plane electric field component.

We start with the analysis of TERS in the absence of graphene, to establish the fundamental phenomena affecting our results. For this study, we focus on the field enhancement induced by the plasmonic system at the position of the molecules. We consider a long finite tip that supports several localized surface plasmon polariton modes, whose wavelengths redshift for smaller gaps between the tip and the sample due to the interaction of the plasmonic tip resonances with the gold substrate. Significantly, a large enhancement of the electromagnetic field normalized by the illumination amplitude is in the range of 30–110 for 1-nm gap, depending on the wavelength of the excitation field. The enhancement is due to both the lightning-rod effect and the plasmonic resonances, and decays very fast as the distance between the tip and the molecular layer increases. Furthermore, the spatial distribution of the fields in the molecular layer shows that the enhancement is strongly confined laterally to a region of about 12 nm, enabling high spatial resolution. Analyzing the integrated Raman signal confirms the importance of a small tip-sample distance to enhance the TERS signal in experimental set-ups.

Interestingly, once we include a graphene layer into the system on top of the molecules we observe only a small change in the electromagnetic enhancement of the Raman signal, even for very high electrostatic doping (large Fermi energy E_F). We believe that this is because graphene surface plasmons are not excited at the large illumination frequencies typical of SERS, thus providing no electromagnetic effect. Beyond the plasmonic mechanism, an additional enhancement could be introduced due to chemical effects (e.g. by charge transfer [12, 13]). Such effects are not covered here but deserve further study.

In contrast with TERS, where illumination by visible or near-infrared light is used, in SEIRA the excitation frequencies are in the mid-infrared spectral region, which corresponds to the energy of graphene plasmons. Thus, we perform calculations to assess if any graphene-related electromagnetic enhancement could arise in SEIRA. Even though we observe an increased enhancement of the field for illumination energies in a spectral window near the condition $\hbar\omega < 2E_F$ both under the tip and also further away (field enhancement for $\lambda = 2100$ nm under the tip is 115 for $E_F = 2$ eV in comparison with 86 when no graphene is present), we think that the acquired results do not point to the excitation of surface plasmons, because we do not obtain such behaviour in a control 2D simulation and because the spatial distribution dependence of the field amplitude in the molecular layer does not correspond to any possible superposition of plasmons (with illuminating wave or with plasmons reflected from a boundary). Hence, the obtained increased field enhancement further away from the tip is probably caused by numerical errors. The enhancement in far-infrared region gradually decreases and becomes even lower than for the case without graphene for which the enhancement stays almost constant. Nonetheless,

including a graphene layer to a plasmonic system and doping it to the right Fermi level can still possibly be used to electromagnetically enhance the field in a selected spectral region in SEIRA experiments (in addition to the chemical enhancement).

In SNOM calculations we utilize a square arrangement of four slits milled in a gold layer on top of a glass substrate as a sample used for formation of a surface plasmon standing wave. The near-field pattern (obtained by illuminating the sample from the bottom side with light linearly polarized along the diagonal of the structure) holds areas with distinct in-plane and out-of-plane electric field component maxima. The SNOM tip (consisting of a tapered glass fiber with a metallic coating with an aperture at the apex) is placed above these maxima in order to investigate the coupling of the respective components into the fiber core as a function of the aperture diameter. We find that for a gold coating the energy flux in the glass core fluctuates with the position in the fiber at which it is measured, suggesting that an energy transfer between the plasmon on the outer surface of the coating and modes inside the probe is a significant addition to the flux. An overall dependence of the component (polarization) selectivity on the diameter of the aperture is observed. A tip with a small aperture with a 60-nm diameter as well as an apertureless tip is more sensitive to the out-of-plane component of the electromagnetic near-field, the sensitivity of a tip with an aperture with a diameter of 120 nm is equally sensitive to both components and a 160-nm aperture tip collects preferentially the in-plane electromagnetic field component.

The results for a SNOM tip with an aluminium coating of the same thickness show strongly suppressed energy transmission through the coating. In consequence, the flux in the tip with the aperture diameter of 120 nm placed above the in-plane component maximum exhibits no oscillations. In the case of the same tip being placed above the out-of-plane component maximum and of a tip with an aperture with 60 nm in diameter the flux is 2–3 orders of magnitude lower and the fluctuations due to energy tunneling through the coating again appear. Even though both tips are more sensitive to the in-plane component, the difference in the sensitivity is lower in the case of the tip with the smaller aperture.

Bibliography

- [1] J. R. Ferraro and K. Nakamoto, *Introductory Raman Spectroscopy*. Academic Press, 2012.
- [2] P. Larkin, *Infrared and Raman Spectroscopy: Principles and Spectral Interpretation*. Elsevier, 2011.
- [3] B. H. Stuart, *Infrared Spectroscopy: Fundamentals and Applications*. John Wiley & Sons, 2004.
- [4] S. A. Maier, *Plasmonics: fundamentals and applications*. Springer Science & Business Media, 1 ed., 2007.
- [5] M. Moskovits, “Surface-enhanced spectroscopy,” *Reviews of Modern Physics*, vol. 57, pp. 783–826, jul 1985.
- [6] S. Nie, “Probing single molecules and single nanoparticles by surface-enhanced raman scattering,” *Science*, vol. 275, pp. 1102–1106, feb 1997.
- [7] P.L. Stiles, J. A. Dieringer, N. C. Shah, and R. P. V. Duyne, “Surface-enhanced raman spectroscopy,” *Annual Review of Analytical Chemistry*, vol. 1, pp. 601–626, jul 2008.
- [8] F. Le, D. W. Brandl, Y. A. Urzhumov, H. Wang, J. Kundu, N. J. Halas, J. Aizpurua, and P. Nordlander, “Metallic nanoparticle arrays: A common substrate for both surface-enhanced raman scattering and surface-enhanced infrared absorption,” *ACS Nano*, vol. 2, pp. 707–718, apr 2008.
- [9] M. Osawa, “Surface-enhanced infrared absorption,” in *Near-Field Optics and Surface Plasmon Polaritons*, pp. 163–187, Springer, 2001.
- [10] A. Campion and P. Kambhampati, “Surface-enhanced raman scattering,” *Chemical Society Reviews*, vol. 27, no. 4, p. 241, 1998.
- [11] R. M. Stöckle, Y. D. Suh, V. Deckert, and R. Zenobi, “Nanoscale chemical analysis by tip-enhanced raman spectroscopy,” *Chemical Physics Letters*, vol. 318, pp. 131–136, feb 2000.
- [12] X. Ling, L. Xie, Y. Fang, H. Xu, H. Zhang, J. Kong, M. S. Dresselhaus, J. Zhang, and Z. Liu, “Can graphene be used as a substrate for raman enhancement?,” *Nano Letters*, vol. 10, pp. 553–561, feb 2010.
- [13] S. Huang, X. Ling, L. Liang, Y. Song, W. Fang, J. Zhang, J. Kong, V. Meunier, and M. S. Dresselhaus, “Molecular selectivity of graphene-enhanced raman scattering,” *Nano Letters*, vol. 15, pp. 2892–2901, may 2015.
- [14] L. Novotny and B. Hecht, *Principles of nano-optics*. Cambridge University Press, 1 ed., 2006.

BIBLIOGRAPHY

- [15] B. Hecht, B. Sick, U. P. Wild, V. Deckert, R. Zenobi, O. J. F. Martin, and D. W. Pohl, “Scanning near-field optical microscopy with aperture probes: Fundamentals and applications,” *The Journal of Chemical Physics*, vol. 112, pp. 7761–7774, may 2000.
- [16] M. Schnell, A. García-Etxarri, A. J. Huber, K. Crozier, J. Aizpurua, and R. Hillenbrand, “Controlling the near-field oscillations of loaded plasmonic nanoantennas,” *Nature Photonics*, vol. 3, pp. 287–291, apr 2009.
- [17] W. L. Barnes, A. Dereux, and T. W. Ebbesen, “Surface plasmon subwavelength optics,” *Nature*, vol. 424, pp. 824–830, aug 2003.
- [18] P. Dvořák, T. Neuman, L. Břínek, T. Šamořil, R. Kalousek, P. Dub, P. Varga, and T. Šikola, “Control and near-field detection of surface plasmon interference patterns,” *Nano Letters*, vol. 13, pp. 2558–2563, may 2013.
- [19] H. G. Frey, S. Witt, K. Felderer, and R. Guckenberger, “High-resolution imaging of single fluorescent molecules with the optical near-field of a metal tip,” *Physical Review Letters*, vol. 93, nov 2004.
- [20] H. F. Hess, E. Betzig, T. D. Harris, L. N. Pfeiffer, and K. W. West, “Near-field spectroscopy of the quantum constituents of a luminescent system,” *Science*, vol. 264, pp. 1740–1745, jun 1994.
- [21] L. Yin, V. K. Vlasko-Vlasov, A. Rydh, J. Pearson, U. Welp, S.-H. Chang, S. K. Gray, G. C. Schatz, D. B. Brown, and C. W. Kimball, “Surface plasmons at single nanoholes in au films,” *Applied Physics Letters*, vol. 85, pp. 467–469, jul 2004.
- [22] Z. Liu, J. M. Steele, W. Srituravanich, Y. Pikus, C. Sun, and X. Zhang, “Focusing surface plasmons with a plasmonic lens,” *Nano Letters*, vol. 5, pp. 1726–1729, sep 2005.
- [23] W. Chen, D. C. Abeysinghe, R. L. Nelson, and Q. Zhan, “Plasmonic lens made of multiple concentric metallic rings under radially polarized illumination,” *Nano Letters*, vol. 9, pp. 4320–4325, dec 2009.
- [24] P. Dvořák, Z. Édes, M. Kvapil, T. Šamořil, F. Ligmajer, M. Hrtoň, R. Kalousek, V. Křápek, P. Dub, J. Spousta, P. Varga, and T. Šikola, “Imaging of near-field interference patterns by aperture-type SNOM – influence of illumination wavelength and polarization state,” *Optics Express*, vol. 25, p. 16560, jul 2017.
- [25] G. M. Lerman, A. Yanai, and U. Levy, “Demonstration of nanofocusing by the use of plasmonic lens illuminated with radially polarized light,” *Nano Letters*, vol. 9, pp. 2139–2143, may 2009.
- [26] W.-I. Lin, F. Shao, B. Stephanidis, and R. Zenobi, “Tip-enhanced raman spectroscopic imaging shows segregation within binary self-assembled thiol monolayers at ambient conditions,” *Analytical and Bioanalytical Chemistry*, vol. 407, pp. 8197–8204, jun 2015.

- [27] W.-I. Lin, M. F. Gholami, P. Beyer, N. Severin, F. Shao, R. Zenobi, and J. P. Rabe, “Strongly enhanced raman scattering of cu-phthalocyanine sandwiched between graphene and au(111),” *Chem. Commun.*, vol. 53, no. 4, pp. 724–727, 2017.
- [28] M. Born and E. Wolf, *Principles of optics: electromagnetic theory of propagation, interference and diffraction of light*. Elsevier, 2013.
- [29] N. W. Ashcroft and N. D. Mermin, *Solid State Physics*. Brooks Cole, 1976.
- [30] P. B. Johnson and R. W. Christy, “Optical constants of the noble metals,” *Physical Review B*, vol. 6, pp. 4370–4379, dec 1972.
- [31] R. H. Ritchie, “Plasma losses by fast electrons in thin films,” *Physical Review*, vol. 106, pp. 874–881, jun 1957.
- [32] A. Otto, “Excitation of nonradiative surface plasma waves in silver by the method of frustrated total reflection,” *Zeitschrift für Physik A Hadrons and nuclei*, vol. 216, pp. 398–410, aug 1968.
- [33] E. Kretschmann, “Die bestimmung optischer konstanten von metallen durch anregung von oberflächenplasmaschwingungen,” *Zeitschrift für Physik A Hadrons and nuclei*, vol. 241, pp. 313–324, aug 1971.
- [34] H. Raether, *Surface Plasmons on Smooth and Rough Surfaces and on Gratings*. Springer Berlin Heidelberg, 1988.
- [35] B. Hecht, H. Bielefeldt, L. Novotny, Y. Inouye, and D. W. Pohl, “Local excitation, scattering, and interference of surface plasmons,” *Physical Review Letters*, vol. 77, pp. 1889–1892, aug 1996.
- [36] K. S. Novoselov, “Electric field effect in atomically thin carbon films,” *Science*, vol. 306, pp. 666–669, oct 2004.
- [37] F. H. L. Koppens, D. E. Chang, and F. J. G. de Abajo, “Graphene plasmonics: A platform for strong light–matter interactions,” *Nano Letters*, vol. 11, pp. 3370–3377, aug 2011.
- [38] K. S. Novoselov, A. K. Geim, S. V. Morozov, D. Jiang, M. I. Katsnelson, I. V. Grigorieva, S. V. Dubonos, and A. A. Firsov, “Two-dimensional gas of massless dirac fermions in graphene,” *Nature*, vol. 438, pp. 197–200, nov 2005.
- [39] J. D. Jackson, *Classical electrodynamics*. John Wiley & Sons, 2007.
- [40] R. Zhang, Y. Zhang, Z. C. Dong, S. Jiang, C. Zhang, L. G. Chen, L. Zhang, Y. Liao, J. Aizpurua, Y. Luo, J. L. Yang, and J. G. Hou, “Chemical mapping of a single molecule by plasmon-enhanced raman scattering,” *Nature*, vol. 498, pp. 82–86, jun 2013.
- [41] L. Ju, B. Geng, J. Horng, C. Girit, M. Martin, Z. Hao, H. A. Bechtel, X. Liang, A. Zettl, Y. R. Shen, and F. Wang, “Graphene plasmonics for tunable terahertz metamaterials,” *Nature Nanotechnology*, vol. 6, pp. 630–634, sep 2011.

BIBLIOGRAPHY

- [42] V. W. Brar, M. S. Jang, M. Sherrott, J. J. Lopez, and H. A. Atwater, “Highly confined tunable mid-infrared plasmonics in graphene nanoresonators,” *Nano Letters*, vol. 13, pp. 2541–2547, jun 2013.
- [43] E. B. Barros and M. S. Dresselhaus, “Theory of raman enhancement by two-dimensional materials: Applications for graphene-enhanced raman spectroscopy,” *Physical Review B*, vol. 90, jul 2014.
- [44] A. E. Klein, N. Janunts, M. Steinert, A. Tünnermann, and T. Pertsch, “Polarization-resolved near-field mapping of plasmonic aperture emission by a dual-SNOM system,” *Nano Letters*, vol. 14, pp. 5010–5015, aug 2014.
- [45] B. N. Tugchinn, N. Janunts, A. E. Klein, M. Steinert, S. Fasold, S. Diziain, M. Sison, E.-B. Kley, A. Tünnermann, and T. Pertsch, “Plasmonic tip based on excitation of radially polarized conical surface plasmon polariton for detecting longitudinal and transversal fields,” *ACS Photonics*, vol. 2, pp. 1468–1475, oct 2015.
- [46] M. Burrelli, D. van Oosten, T. Kampfrath, H. Schoenmaker, R. Heideman, A. Leinse, and L. Kuipers, “Probing the magnetic field of light at optical frequencies,” *Science*, vol. 326, pp. 550–553, oct 2009.
- [47] D. K. Singh, J. S. Ahn, S. Koo, T. Kang, J. Kim, S. Lee, N. Park, and D.-S. Kim, “Selective electric and magnetic sensitivity of aperture probes,” *Optics Express*, vol. 23, p. 20820, jul 2015.
- [48] B. le Feber, N. Rotenberg, D. M. Beggs, and L. Kuipers, “Simultaneous measurement of nanoscale electric and magnetic optical fields,” *Nature Photonics*, vol. 8, pp. 43–46, dec 2013.
- [49] K. Walzer, E. Marx, N. C. Greenham, R. J. Less, P. R. Raithby, and K. Stokbro, “Scanning tunneling microscopy of self-assembled phenylene ethynylene oligomers on au(111) substrates,” *Journal of the American Chemical Society*, vol. 126, pp. 1229–1234, feb 2004.
- [50] E. Marx, K. Walzer, R. J. Less, P. R. Raithby, K. Stokbro, and N. C. Greenham, “Optical constants and self-assembly of phenylene ethynylene oligomer monolayers,” *Organic Electronics*, vol. 5, pp. 315–320, dec 2004.
- [51] M. K. Schmidt, R. Esteban, F. Benz, J. J. Baumberg, and J. Aizpurua, “Linking classical and molecular optomechanics descriptions of SERS,” *Faraday Discuss.*, 2017.
- [52] R. Carminati, M. Nieto-Vesperinas, and J.-J. Greffet, “Reciprocity of evanescent electromagnetic waves,” *Journal of the Optical Society of America A*, vol. 15, p. 706, mar 1998.
- [53] A. D. Rakić, “Algorithm for the determination of intrinsic optical constants of metal films: application to aluminum,” *Applied Optics*, vol. 34, p. 4755, aug 1995.
- [54] “The Finite Element Method (FEM).”
<http://www.comsol.com/multiphysics/finite-element-method/>. Retrieved on 2017-06-25.

- [55] COMSOL Multiphysics[®], COMSOL Inc. <http://www.comsol.com/>.
- [56] L. K. Khorashad, L. V. Besteiro, Z. Wang, J. Valentine, and A. O. Govorov, “Localization of excess temperature using plasmonic hot spots in metal nanostructures: Combining nano-optical antennas with the fano effect,” *The Journal of Physical Chemistry C*, vol. 120, pp. 13215–13226, jun 2016.
- [57] B. E. A. Saleh and M. C. Teich, *Fundamentals of Photonics*. Wiley-Interscience, 2007.

Appendices

A. Analytical model for a multilayer system

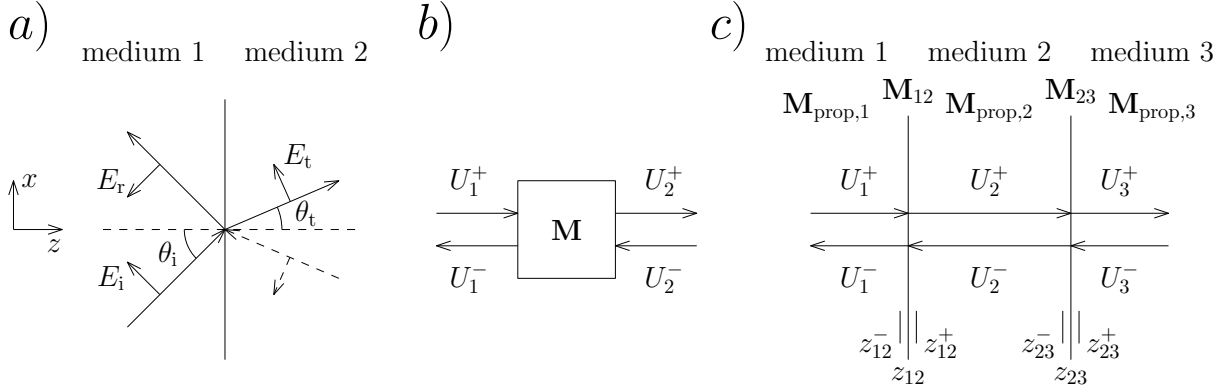


Figure A.1: Sketches indicating the notation used in the transfer-matrix method. (a) Reflection at an interface, where we indicate the direction of the electric field (and of wave propagation) that we use. We indicate the incident (E_i), reflected (E_r) and transmitted (E_t) field, together with the incident (θ_i) and transmitted (θ_t) angle. In general, one can also consider a plane wave incident to the interface from the other side, which is represented by the dashed oblique line. We also indicate the coordinate axes used in this appendix. (b) Notation used in the transfer-matrix method. The plane waves are represented by the amplitude U_m^\pm , where the subindex indicate the medium, and “+” and “-” correspond to waves propagating towards the right and towards the left, respectively (the plane wave used as excitation of the full system would correspond to U_1^+). (c) Scheme of a multilayer system consisting of three media. $\mathbf{M}_{\text{prop},m}$ are matrices of propagation through a medium m and $\mathbf{M}_{m,m+1}$ are matrices describing interfaces $m,m+1$ at positions $z_{m,m+1}$. We distinguish between $z_{m,m+1}^-$ and $z_{m,m+1}^+$ to differentiate between the fields excited just to the left and just to the right of the interface, respectively.

To obtain the response of a multilayer system, we have implemented the transfer-matrix method [57]. We first consider the situation at an interface separating two media. We indicate in Fig. A.1a the orientation of the fields for a single interface illuminated by a plane wave; in principle, we could choose the opposite orientation - or, equivalently, sign - of some of the fields, but it would be necessary to take into account how this change modifies the sign in the equations.

The notation to use in the following is indicated in Fig. A.1b. The system can be illuminated by an incoming plane wave from either of the two media (amplitude U_1^+ and U_2^- for medium 1 (on the left) and 2 (on the right), respectively). The illumination induces two plane waves outgoing from the interface (amplitudes U_1^- and U_2^+ for medium 1 and 2, respectively). The amplitudes of the reflected and transmitted wave are connected with the incident wave by the scattering matrix \mathbf{S}

$$\begin{pmatrix} U_2^+(z_{12}^+) \\ U_1^-(z_{12}^-) \end{pmatrix} = \mathbf{S}_{12} \begin{pmatrix} U_1^+(z_{12}^-) \\ U_2^-(z_{12}^+) \end{pmatrix} = \begin{pmatrix} t_{12} & r_{21} \\ r_{12} & t_{21} \end{pmatrix} \begin{pmatrix} U_1^+(z_{12}^-) \\ U_2^-(z_{12}^+) \end{pmatrix}, \quad (\text{A.1})$$

where by z_{12}^- (z_{12}^+) we indicate that the amplitude is evaluated just to the left (right) of the interface situated at position z_{12} , t_{12} and r_{12} are the transmission and reflection

A. ANALYTICAL MODEL FOR A MULTILAYER SYSTEM

coefficients for a wave coming from medium 1 towards medium 2 and t_{21} and r_{21} are the corresponding values for the opposite direction. For p-polarization (that we use in all calculations in this thesis) the Fresnel coefficients are (Eq. 1.9):

$$\begin{aligned} r_{12} &= \frac{\varepsilon_2 k_{1z} - \varepsilon_1 k_{2z} + \frac{\sigma_{\text{gph}}}{\varepsilon_0 \omega} k_{1z} k_{2z}}{\varepsilon_2 k_{1z} + \varepsilon_1 k_{2z} + \frac{\sigma_{\text{gph}}}{\varepsilon_0 \omega} k_{1z} k_{2z}}, \\ t_{21} &= \frac{2\varepsilon_1 \frac{k_{1z} k_2}{k_1}}{\varepsilon_2 k_{1z} + \varepsilon_1 k_{2z} + \frac{\sigma_{\text{gph}}}{\varepsilon_0 \omega} k_{1z} k_{2z}}, \end{aligned} \quad (\text{A.2})$$

where k_1 and k_2 are the wave vectors in the two media (with permittivity ε_1 and ε_2 , respectively) and k_{1z} and k_{2z} are their normal components. In order to obtain the solution of a multilayer system, we need to consider a succession of interfaces. With this aim, it is convenient to transform the scattering matrix \mathbf{S} into a wave-transfer matrix \mathbf{M} that relate the amplitudes on one side (U_2^+, U_2^-) to those on the other side (U_1^+, U_1^-)

$$\begin{pmatrix} U_2^+(z_{12}^+) \\ U_2^-(z_{12}^+) \end{pmatrix} = \mathbf{M}_{12} \begin{pmatrix} U_1^+(z_{12}^-) \\ U_1^-(z_{12}^-) \end{pmatrix} = \begin{pmatrix} A & B \\ C & D \end{pmatrix} \begin{pmatrix} U_1^+(z_{12}^-) \\ U_1^-(z_{12}^-) \end{pmatrix}. \quad (\text{A.3})$$

The conversion relations between the scattering and wave-transfer matrices are

$$\mathbf{M}_{12} = \begin{pmatrix} A & B \\ C & D \end{pmatrix} = \frac{1}{t_{21}} \begin{pmatrix} t_{12} t_{21} - r_{12} r_{21} & r_{21} \\ -r_{12} & 1 \end{pmatrix}, \quad (\text{A.4})$$

$$\mathbf{S}_{12} = \begin{pmatrix} t_{12} & r_{21} \\ r_{12} & t_{21} \end{pmatrix} = \frac{1}{D} \begin{pmatrix} AD - BC & B \\ -C & 1 \end{pmatrix}. \quad (\text{A.5})$$

Besides the interfaces, we also need to consider the propagation through a medium m over a distance $z - z_{m-1,m}$ from the previous interface (situated at $z_{m-1,m}$). The corresponding scattering and wave-transfer matrices are

$$\mathbf{S}_{\text{prop},m}(z - z_{m-1,m}) = \begin{pmatrix} e^{ik_m, z(z-z_{m-1,m})} & 0 \\ 0 & e^{ik_m, z(z-z_{m-1,m})} \end{pmatrix}, \quad (\text{A.6})$$

$$\mathbf{M}_{\text{prop},m}(z - z_{m-1,m}) = \begin{pmatrix} e^{ik_m, z(z-z_{m-1,m})} & 0 \\ 0 & e^{-ik_m, z(z-z_{m-1,m})} \end{pmatrix}. \quad (\text{A.7})$$

Thus, if we consider the layer m between the interfaces at $z_{m-1,m}$ and $z_{m,m+1}$, the amplitudes at both ends of this layer are connected by

$$\begin{pmatrix} U_m^+(z_{m,m+1}^-) \\ U_m^-(z_{m,m+1}^-) \end{pmatrix} = \begin{pmatrix} e^{ik_m, z(z_{m,m+1}-z_{m-1,m})} & 0 \\ 0 & e^{-ik_m, z(z_{m,m+1}-z_{m-1,m})} \end{pmatrix} \begin{pmatrix} U_m^+(z_{m-1,m}^+) \\ U_m^-(z_{m-1,m}^+) \end{pmatrix}. \quad (\text{A.8})$$

As the matrices connect the amplitudes at both sides of one of the interfaces (Eq. A.3) or of the layers (Eq. A.8), the wave-transfer matrices can be combined by multiplying them

in reverse order. Considering for example a system with three media and two interfaces (Fig. A.1c)

$$\begin{aligned}
\begin{pmatrix} U_3^+(z_{23}^+) \\ U_3^-(z_{23}^+) \end{pmatrix} &= \mathbf{M}_{23} \begin{pmatrix} U_2^+(z_{23}^-) \\ U_2^-(z_{23}^-) \end{pmatrix} \\
&= \mathbf{M}_{23} \mathbf{M}_{\text{prop},2}(z_{23} - z_{12}) \begin{pmatrix} U_2^+(z_{12}^+) \\ U_2^-(z_{12}^+) \end{pmatrix} \\
&= \mathbf{M}_{23} \mathbf{M}_{\text{prop},2}(z_{23} - z_{12}) \mathbf{M}_{12} \begin{pmatrix} U_1^+(z_{12}^-) \\ U_1^-(z_{12}^-) \end{pmatrix}
\end{aligned} \tag{A.9}$$

gives the total wave-transfer matrix \mathbf{M} between medium 1 and 3, \mathbf{M}_{13} , as:

$$\mathbf{M}_{13} = \mathbf{M}_{23} \mathbf{M}_{\text{prop},2}(z_{23} - z_{12}) \mathbf{M}_{12} . \tag{A.10}$$

In this way we can obtain the total transmission (t_{tot}) and reflection (r_{tot}) coefficients for a multilayer system by calculating the total wave-transfer matrix \mathbf{M} and using Eq. A.5. The amplitude of the plane wave reflected from the whole multilayer system is then $U_1^-(z_{12}^-) = r_{\text{tot}} U_1^+(z_{12}^-)$ (with $U_1^+(z_{12}^-)$ being the amplitude of the incident wave). From $U_1^+(z_{12}^-)$ and $U_1^-(z_{12}^-)$, we can express the amplitude of the field in any arbitrary point in medium n at position z as

$$\begin{pmatrix} U_n^+(z) \\ U_n^-(z) \end{pmatrix} = \mathbf{M}_{\text{prop},n}(z - z_{n-1,n}) \mathbf{M}_{n-1,n} \cdots \mathbf{M}_{12} \begin{pmatrix} U_1^+(z_{12}^-) \\ U_1^-(z_{12}^-) \end{pmatrix} , \tag{A.11}$$

with $z - z_{n-1,n}$ indicating the distance from the closest interface to the left (at $z_{n-1,n}$).

From the values of the amplitude of the plane waves propagating forwards (U_n^+) and backwards (U_n^-), we can readily obtain the x and z components of the fields at position z in layer n , as:

$$\begin{aligned}
E_x(z) &= (U_n^+(z) - U_n^-(z)) \frac{k_{n,z}}{k_n} , \\
E_z(z) &= -(U_n^+(z) + U_n^-(z)) \frac{q}{k_n} ,
\end{aligned} \tag{A.12}$$

where q , $k_{n,z}$ and k_n correspond to the parallel component, the normal component, and the amplitude of the wave vector, respectively. The factors $k_{n,z}/k_n$ and q/k_n take into account that the angle of propagation in each medium depends on its dielectric constant according to Snell's law. The signs in Eq. A.12 correspond to the convention of field orientation in Fig. A.1a (which also sets the sign of the reflection and transmission coefficient in Eq. A.2).